JGR Atmospheres

RESEARCH ARTICLE
10.1029/2018JD029596

Cloud-Resolving Model Intercomparison of an MC3E Squall Line Case: Part II. Stratiform Precipitation Properties

Bin Han[1,2], Jiwen Fan[2], Adam Varble[2,3], Hugh Morrison[4], Christopher R. Williams[5], Baojun Chen[1], Xiquan Dong[6], Scott E. Giangrande[7], Alexander Khain[8], Edward Mansell[9], Jason A. Milbrandt[10], Jacob Shpund[8], and Gregory Thompson[4]

[1]School of Atmospheric Sciences, Nanjing University, Nanjing, China, [2]Pacific Northwest National Laboratory, Richland, WA, USA, [3]Department of Atmospheric Sciences, University of Utah, Salt Lake City, UT, USA, [4]National Center for Atmospheric Research, Boulder, CO, USA, [5]Cooperative Institute for Research in Environmental Sciences, University of Colorado Boulder and NOAA/Earth System Research Laboratory, Boulder, CO, USA, [6]Department of Hydrology and Atmospheric Sciences, University of Arizona, Tucson, Arizona, USA, [7]Environmental and Climate Sciences Department, Brookhaven National Laboratory, Upton, NY, USA, [8]The Institute of the Earth Science, The Hebrew University of Jerusalem, Jerusalem, Israel, [9]NOAA/OAR/National Severe Storms Laboratory, Norman, OK, USA, [10]Meteorological Research Division, Environment and Climate Change Canada, Dorval, Canada

Abstract In this second part of a cloud microphysics scheme intercomparison study, we focus on biases and variabilities of stratiform precipitation properties for a midlatitude squall line event simulated with a cloud-resolving model implemented with eight cloud microphysics schemes. Most of the microphysics schemes underestimate total stratiform precipitation, mainly due to underestimation of stratiform precipitation area. All schemes underestimate the frequency of moderate stratiform rain rates (2–6 mm/hr), which may result from low-biased ice number and mass concentrations for 0.2–2-mm diameter particles in the stratiform ice region. Most simulations overestimate ice water content (IWC) at altitudes above 7 km for temperatures colder than −20 °C but produce a decrease of IWC approaching the melting level, which is opposite to the trend shown by in situ observations. This leads to general underestimations of stratiform IWC below 5-km altitude and rainwater content above 1-km altitude for a given rain rate. Stratiform precipitation area positively correlates with the convective condensate detrainment flux but is modulated by hydrometeor type, size, and fall speed. Stratiform precipitation area also changes by up to 17%–25% through alterations of the lateral boundary condition forcing frequency. Stratiform precipitation, rain rate, and area across the simulations vary by a factor of 1.5. This large variability is primarily a result of variability in the stratiform downward ice mass flux, which is highly correlated with convective condensate horizontal detrainment strength. The variability of simulated local microphysical processes in the stratiform region plays a secondary role in explaining variability in simulated stratiform rainfall properties.

Plain Language Summary This is a unique model intercomparison study about different microphysics parametrizations commonly used, with the purposes of examining model biases and variability as well as identifying major factors/processes leading to bias and variability. The study simulated a well-observed squall line MCS from MC3E field campaign, and focused on the stratiform precipitation, following on our part 1 study focusing on convective part. We employed a more constrained approach compared with past intercomparison studies to better identify processes contributing to the differences. Another unique part is our comprehensive model evaluation, that is, we identify stratiform columns and evaluate vertical evolution of cloud properties including size distribution. We find that most of the microphysics schemes underestimate total stratiform precipitation, mainly due to underestimation of stratiform precipitation area. Moderate stratiform rain rates are underestimated, mainly due to incorrect vertical evolution of ice particles. Stratiform precipitation properties across the simulations vary by a factor of 1.5, primarily a result of variability in detrained condensate amount. In addition, we find that stratiform precipitation area correlates well with detrainment amount and is modulated by the detrained hydrometeor properties. So convective microphysics plays a key role in determining stratiform properties.

Key Points:
- Underestimation of total stratiform precipitation in most simulations is mainly due to underestimation of stratiform precipitation area
- Low-biased rainwater content is caused by low-biased stratiform ice water content below 5-km altitude for a given rain rate
- Simulated stratiform precipitation variability is correlated with variability in the convective condensate being detrained

Supporting Information:
- Supporting Information S1

Correspondence to:
J. Fan and B. Chen,
jiwen.fan@pnnl.gov;
bjchen@nju.edu.cn

Citation:
Han, B., Fan, J., Varble, A., Morrison, H., Williams, C. R., Chen, B., et al. (2019). Cloud-resolving model intercomparison of an MC3E squall line case: Part II. Stratiform precipitation properties. *Journal of Geophysical Research: Atmospheres*, *124*, 1090–1117. https://doi.org/10.1029/2018JD029596

Received 11 SEP 2018
Accepted 20 DEC 2018
Accepted article online 2 JAN 2019
Published online 29 JAN 2019

1. Introduction

Mesoscale convection systems (MCSs) produce a large proportion of precipitation in both tropical and midlatitude regions (Houze, 2004). The dynamic and thermodynamic features of MCSs have been widely studied through radar-based observations (e.g., Braun & Houze, 1994; Houze, 1977; Parker & Johnson, 2000; Smith et al., 2009; Smull & Houze, 1987). More recent field campaign studies using coincident aircraft measurements and dual-polarization radar quantities have focused on fingerprinting key microphysical processes such as aggregation and riming in the trailing stratiform rain regions of MCSs (Giangrande et al., 2016; Kumjian et al., 2016). However, accurately simulating some well-observed kinematic and microphysical features of MCSs has been challenging. Although cloud-resolving models (CRMs) benefit from finer grid resolution and more sophisticated physical parameterizations than coarser-resolution numerical weather prediction and global climate models, they still have deficiencies in accurately representing the internal kinematic and microphysical structure of MCSs (e.g., Bernardet et al., 2000; Franklin et al., 2016; Marinescu et al., 2016; Tao et al., 2016; Weisman et al., 2008; Wu et al., 2013).

The causes of discrepancies between observations and model simulations at cloud-resolving scales can be very complicated. Errors in initial conditions, resolved dynamics and thermodynamics, physics parameterizations such as aerosol and cloud microphysics schemes, and complex interactions and feedbacks between these factors can all contribute to model biases. Extensive observational data from field campaigns provide good opportunities to evaluate MCS simulations, particularly with different cloud microphysics parameterizations that have been shown to cause significant model spread (e.g., Fan et al., 2015, 2017; Lang et al., 2007; Li et al., 2008; Stanford et al., 2017; Varble et al., 2011, 2014a, 2014b; Xu et al., 2002). Previous studies document a common high bias in convective radar reflectivity mainly caused by excessive amounts of large ice particles aloft. While the magnitude of this bias is related to the manner in which hydrometeor properties are parameterized, it is also related to vertical velocities above the melting level that are high biased in comparison with multi-Doppler-retrieved wind fields (Fan et al., 2015, 2017; Varble et al., 2014a). Stanford et al. (2017) speculate that insufficient parameterization of mixed phase processes may also contribute to this bias. Overall, CRMs exhibit significant biases and model spread in simulated deep convective kinematic and microphysical properties for numerous well-observed cases around the world.

Simulating stratiform regions of MCSs is also problematic. Although CRMs can qualitatively simulate some cloud properties in stratiform region, underestimation of stratiform precipitation has been a long-standing model issue (e.g., Fovell & Ogura, 1988; Franklin et al., 2016; Fridlind et al., 2017; Luo et al., 2010; Morrison et al., 2015; Varble et al., 2011, 2014b). Past studies also show that simulated stratiform regions tend to be narrower than observed (e.g., Fovell & Ogura, 1988; Fridlind et al., 2017; Lang et al., 2003; McCumber et al., 1991; Varble et al., 2014b; Wu et al., 2013). Reasons for the consistent underestimation of stratiform precipitation are not well understood, but studies have shown that parameterization of rain microphysics could play an important role. For example, Li et al. (2009) show that the fixed raindrop size intercept parameter (N_0) of an assumed exponential raindrop size distribution (RSD) in a one-moment bulk microphysics scheme can lead to excessive rain evaporation and cause an underestimation of stratiform surface rainfall. Greater flexibility in representing the RSD through multimoment and explicit bin approaches limits this bias, which results in wider stratiform precipitation area (SPA; e.g., Khain et al., 2015; Morrison et al., 2009). In addition, Varble et al. (2014b) found that underestimated stratiform precipitation rate was correlated with likely underestimated ice water content (IWC) at the melting level. Due to strong connections between convective and stratiform regions in MCSs (Biggerstaff & Houze, 1991; Ferrier et al., 1996; Rutledge & Houze, 1987; Tao et al., 1993), model biases in the stratiform region can be caused by unrealistic convective properties. Blossey et al. (2007) suggest that simulated convective precipitation efficiency may be too great, possibly reducing stratiform precipitation relative to observed. Luo et al. (2010) and Varble et al. (2014b) point out that the underestimation of stratiform rainfall could be partly associated with biases in the magnitude and altitude of detrainment from convective regions. However, Bryan and Morrison (2012) showed that the underestimation of stratiform precipitation could also be associated with the lack of detrainment owing to poorly resolved convective updrafts in kilometer-scale models. In general, models frequently fail to reproduce observed MCS stratiform region properties for a range of complicated reasons. Model-observation comparisons for stratiform properties require further examination to improve our understanding of the primary causes of simulation bias and spread to provide insights for model improvement.

Comprehensive observations of a squall line event during the Midlatitude Continental Convective Clouds Experiment (MC3E) field campaign (Jensen et al., 2016) provide an excellent opportunity to systematically evaluate simulated stratiform precipitation properties. In addition, many previous model intercomparison studies used different models, making it difficult to attribute model differences to specific microphysics factors (e.g., Varble et al., 2011; Xu et al., 2002). Therefore, we carry out this intercomparison study with a constrained approach by using the same CRM while only changing microphysics parameterizations. Following Part I that focused on convective properties (Fan et al., 2017), we evaluate simulated stratiform precipitation properties against in situ and remote sensing retrievals. Potential reasons are explored for stratiform precipitation property variability across a range of microphysics schemes used in the intercomparison simulations. Detailed descriptions of the observations used in this study are presented in section 2. Simulation design and the intercomparison methodology are described in sections 3 and 4, respectively. In section 5, we present the main results, including comparison of stratiform precipitation properties with observations and intercomparison of simulations to explore potential key processes responsible for model variabilities and biases. Section 6 summarizes the study and presents main conclusions.

2. Observations

The simulations in this study focus on the squall line event that occurred on 20 May 2011 during the MC3E field campaign. This event is well described by Jensen et al. (2016). The deep convective region of the squall line passed over the Atmospheric Radiation Measurement (ARM; Mather & Voyles, 2013) Southern Great Plains (SGP) Central Facility (CF) between 1030 and 1100 UTC. Following the convective precipitation, a wide stratiform precipitation region passed over the site (Figure 1a) and was well observed by ground-based instruments and aircraft measurements (Figures 1b and 1c).

There were 16 Parsivel disdrometers (Thurai et al., 2011; Tokay et al., 2013) and one 2-D video disdrometer (2DVD; Schönhuber et al., 2008) in the vicinity of the SGP site that provide stratiform surface rain rate and RSD information for this case (Figure 1c). The 2DVD data were collected over 41-diameter bins from 0.1 to 10 mm, and Parsivel data were collected over 32-diameter bins from 0.06 to 25.2 mm. Both disdrometer observations have 1-min temporal resolution. This translates to approximately 1-km spatial resolution when considering the typical propagation speed of the squall line as ~15 m/s. According to Tokay et al. (2013), the 2DVD observations show good agreement with rain gauge measurements in total rainfall, whereas the Parsivel disdrometers have a low bias in number concentrations for small raindrops less than 0.76 mm in diameter and a high bias in number concentrations for raindrops with sizes larger than 2.44 mm in diameter. Further details of these disdrometers can be found in Jensen et al. (2016) and Tokay et al. (2017).

To better understand the vertical evolution of stratiform microphysical properties, vertically pointing radar (VPR) data are employed. VPRs were operated at 449 MHz (UHF) and 2,835 MHz (S-band) at the SGP CF in north central Oklahoma (Figure 1c). S-band vertical profiler provides Rayleigh radar reflectivity and Doppler velocity data, while the UHF vertical profiler additionally observes Bragg scattering related to the vertical air motion (Williams, 2016). To estimate the vertical air motion more precisely, Williams (2012) developed a dual-frequency retrieval technique to subtract the Rayleigh scattering signal in one VPR spectra from the other spectra that contains both Rayleigh and Bragg scattering signals. VPR spectra are also used to retrieve RSDs between ~0.5- and 3-km altitude following the dual-frequency retrieval technique in Williams and Gage (2009). A three-parameter gamma distribution is used to fit the RSDs with the form:

$$N(D) = N_0 D^{\mu} e^{-\lambda D}, \tag{1}$$

where D is the particle diameter, N_0 is the intercept parameter, μ is the shape parameter, and λ is the slope parameter. Microphysical variables such as rainwater content (RWC) and mass-weighted mean diameter (D_m) are then retrieved using moments of the gamma RSD. Detailed application of dual-frequency retrieval technique and calibration processes for this case are in Williams (2016). When the aircraft was flying near the SGP CF, the VPR-retrieved RWC agrees well with the aircraft-retrieved liquid water content just below the melting level.

In addition to vertical air motion retrieved by the VPRs, we utilize a multi-Doppler radar 3-D wind field retrieval as described in Part I to evaluate the zonal wind in the stratiform region. Radial velocity

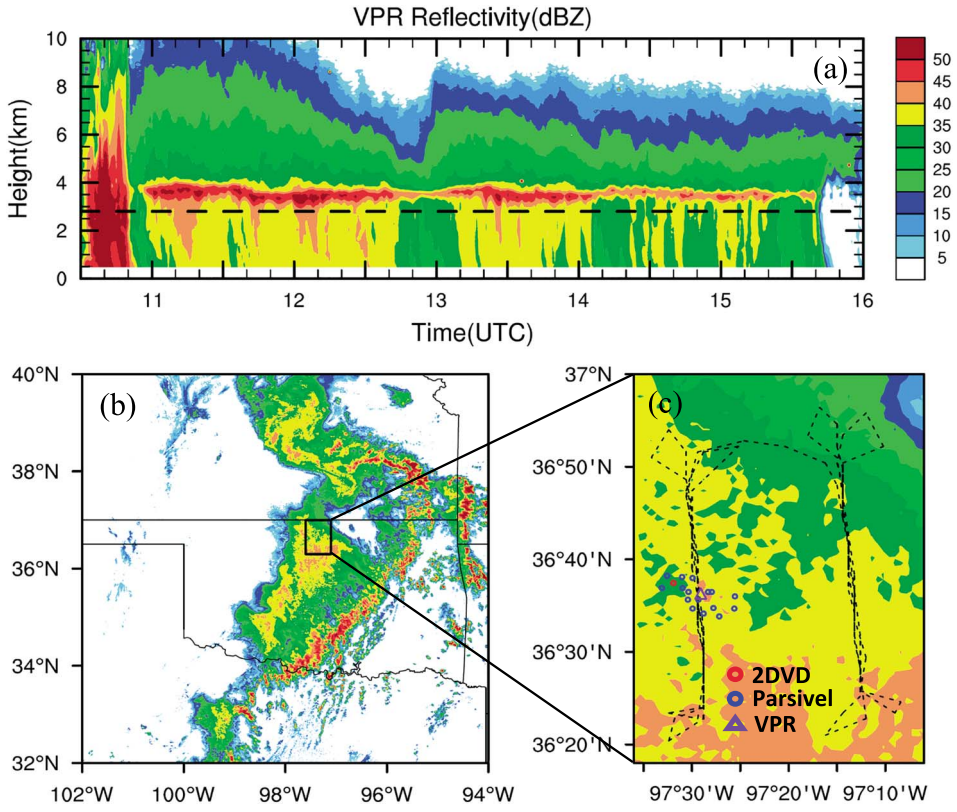

Figure 1. (a) Time-height cross section of S-band vertical profiler reflectivity (dBZ) from 1030 to 1600 UTC on 20 May 2011 at the ARM SGP CF. The black dashed line represents the maximum height of vertical profiler retrievals of stratiform rain properties. (b) The 2.5-km altitude NEXRAD radar reflectivity at 1330 UTC. (c) Location of ground-based observations (colored markers) and aircraft flight tracks from 1335 to 1515 UTC (dashed black line). The zoomed-in domain in (c) is the black box in (b), and the radar reflectivity in (b) and (c) has the same color bar as in (a). Note that radar reflectivity in (b and c) is at a fixed time, while the aircraft flight tracks overlaid in (c) are during a time period.

observations from a 6.3-GHz C-band Scanning ARM Precipitation Radar (e.g., Giangrande et al., 2014) located ~20 km north of the SGP CF and Next Generation Radar (NEXRAD) WSR-88D 2.8-GHz (S-band) radars (e.g., Whiton et al., 1998) located at Vance Air Force Base, OK (KVNX), and Wichita, KS (KICT), were assimilated in a three-dimensional variational algorithm to retrieve the 3-D wind field (North et al., 2017). Additionally, vertical profiles of temperature and relative humidity data at 10-min frequency retrieved from Raman lidar measurements are used to characterize the thermodynamic characteristics of the observed stratiform region below the melting level. The Raman lidar was operated at the SGP CF, and detailed measurement methods are provided by Newsom et al. (2013).

Aircraft in situ measurements and NOAA NEXRAD retrievals are used to characterize stratiform ice properties. The Citation II aircraft started to sample the stratiform precipitation region at about 1300 UTC and flew at subfreezing temperatures from 1335 to 1515 UTC with two primary tracks (Figure 1c). The first flight track (1335–1420 UTC) was over and near the aforementioned ground-based instruments. The second flight track (1420–1515 UTC) was about 30 km east of the first track and measured a lesser rain rate region. The first track is matched with surface-based observations in our analyses. According to previous studies (e.g., Korolev et al., 1998; Korolev et al., 2013), the Nevzorov probe aboard the Citation II aircraft likely underestimated IWC for large particles due to its limited sensing area. Therefore, we instead use the best estimated IWC described in Wang et al. (2015) that combines 2-Dimensional Cloud optical array probe (2 DC) and High-Volume Precipitation Spectrometer measurements (i.e., ice particle number size distribution data) and assumes a mass-size relationship $M = a\,D^b$, where $a = 0.00365$ and $b = 2.1$.

NEXRAD-retrieved IWC data are used for evaluating stratiform ice microphysical properties over a broader area than is possible with the aircraft in situ measurements. The ice cloud microphysical

properties for the stratiform precipitation and thick anvil regions of deep convective systems are retrieved using NEXRAD radar reflectivity and empirical relationships from aircraft in situ measurements during MC3E (Tian et al., 2016). It is horizontally gridded at 0.02° (~2 km) with 1-km vertical resolution. The 5-min time frequency is the same as the NEXRAD data set used. Significant aggregation of snow likely occurs at relatively warm temperatures between −10 °C and 0 °C, causing an increase in particle size without an increase in IWC, which can make the reflectivity-IWC relationship invalid at these temperatures. Therefore, our evaluation focuses on temperatures colder than −12 °C (about 6-km altitude and above).

For the evaluation of stratiform precipitation properties over a broad area, three surface precipitation products that combine radar and rain gauge measurements are used. These data sets are the NEXRAD National Mosaic and Multi-sensor Quantitative Precipitation Estimate (NMQ Q2), a bias-corrected NEXRAD Q2 (Q2_GAUGE), and an hourly Arkansas-Red Basin River Forecast Center (ABRFC) product (e.g., Young et al., 2000; Zhang et al., 2011). The NMQ Q2 product is based on a conventional radar reflectivity-rain rate relationship that commonly overestimates rainfall accumulation during Oklahoma's warm season (e.g., Giangrande & Ryzhkov, 2008; Gourley et al., 2010; Stenz et al., 2014; Wang et al., 2016; Wang et al., 2018). The bias-corrected Q2 and ABRFC products that incorporate surface rain gauge measurements can reduce the accumulation errors in rainfall estimates. Therefore, these two products better represent the observational hourly precipitation in the stratiform region. Detailed descriptions of these precipitation data sets can be found in Part I.

3. Simulations

The Advanced Research Weather Research and Forecasting (WRF) model version 3.4.1 (Skamarock et al., 2008) is used for this intercomparison study. Simulations use four domains, and the innermost domain covers an area of 601 km × 511 km with 1-km horizontal grid spacing (see Figure 1 of Part I). Simulations of Domain 4 are performed separately using a one-way nested down approach with lateral boundary conditions provided by Domain 3 every 3 hr. Eight microphysics schemes are used in this study: Morrison (MORR), Milbrandt and Yau (MY2), WSM6 (WSM6), National Severe Storms Laboratory (NSSL), Predicted Particle Properties (P3), Thompson (THOM) Bulk Microphysics, Fast Spectral-Bin Microphysics (FSBM), and the new Fast Spectral-Bin Microphysics version (FSBM_NEW). References and prognostic variables for each microphysics scheme are listed in Table 1. The Texas A&M University (TAMU) Bulk Microphysics considered in Part I is not included because of unrealistic size and fall speed produced for graupel in the stratiform region. Further development and modifications are being implemented for the TAMU scheme. Other detailed descriptions of model configuration and microphysics schemes can be found in Part I.

The reasons for adding a simulation with FSBM_NEW are twofold. First, a couple of tuning parameters in the FSBM simulation were set to values that are not realistic for stratiform cloud properties (discussed in the section 5). Second, FSBM_NEW performs relatively well for the same MCS event using a two-way nesting option. Using it in this study serves the purpose of evaluating its performance with the one-way nesting setup. FSBM_NEW has 33 and 43 bin options. The 33-bin version is chosen here for consistency with the 33-bin FSBM version. FSBM_NEW has several major differences with FSBM. First, pressure adjusted hydrometeor fall speeds are employed for the ventilation of various particles during the diffusional growth/evaporation processes rather than only for the sedimentation process alone in FSBM. Second, the collision-coalescence kernels are corrected to take the pressure (density) effect into account. Third, a new cloud base nucleation parameterization is employed, which results in higher nucleation rate. Lastly, snow particle breakup is applied to the relatively larger size bins with lower breakup probabilities compared with those in FSBM.

4. Intercomparison Methodology

4.1. Analysis Time Period and Domain

The time-height cross section of radar reflectivity from the S-band profiler shows that the well-defined stratiform precipitation region of the squall line passed over the instruments around the SGP site from 1100 to 1400 UTC (Figure 1a). After 1400 UTC, the *bright band* feature of radar reflectivity became weaker and

Table 1
Summary of the Microphysics Schemes Employed in This Study

Microphysics	Approach	[b] Prognostic variables	References
MORR	Two-moment	Q_c, Q_r, Q_i, Q_s, Q_h, N_r, N_i, N_s, N_h	Morrison et al. (2005, 2009)
MY2	Two-moment	Q_c, Q_r, Q_i, Q_s, Q_g, Q_h, N_r, N_i, N_s, N_g, N_h	Milbrandt and Yau (2005a, 2005b), Milbrandt and McTaggart-Cowan (2010), and Milbrandt et al. (2012)
WSM6	One-moment	Q_c, Q_r, Q_i, Q_s, Q_g	Hong and Lim (2006)
FSBM	Bin-resolved	Q_c, Q_r, Q_i, Q_s, Q_h, N_c, N_r, N_i, N_s, N_h	Khain (2009) and Fan et al. (2012)
NSSL	Two-moment	Q_c, Q_r, Q_i, Q_s, Q_g, Q_h, N_c, N_r, N_i, N_s, N_g, N_h, V_g, V_h	Mansell et al. (2010)
[a] P3	Two-moment	Q_c, Q_r, Q_{i_tot}, Q_{i_rim}, B_{i_rim}, N_r, N_{i_tot},	Morrison and Milbrandt (2015)
THOM	Hybrid one- and two-moment	Q_c, Q_r, Q_i, Q_s, Q_g, N_r, N_i	Thompson et al. (2004, 2008)
FSBM_NEW	Bin-resolved	Q_c, Q_r, Q_i, Q_s, Q_h, N_c, N_r, N_i, N_s, N_h	Modified based on FSBM

[a] Q_{i_rim} and B_{i_rim} denote the riming mass and volume mixing ratios, respectively. [b] Symbols denote the mass and number mixing ratios of cloud water (Q_c, N_c), rain (Q_r, N_r), ice (Q_i, N_i), snow (Q_s, N_s), graupel (Q_g, N_g), and hail (Q_h, N_h). In P3, cloud ice includes all ice types and is characterized by rimed mass fraction. V_g and V_h are volume mixing ratios for predicting bulk density for graupel and hail, respectively.

the radar echo top height also decreased. Therefore, 1100–1400 UTC is chosen as the primary analysis time period for observations. For simulations, model output data from the innermost domain between 1000 and 1300 UTC are used. The 1-hr lag between the simulations and observations is justified in Part I based on faster MCS development in simulations than observations.

In order to match the northeast-southwest orientation of observed and simulated squall lines, the analysis region is parallelogram-shaped (Figure 2). The parallelogram areas are set to follow the movement of the observed and simulated systems during their corresponding analysis time period. Each parallelogram has the same size that covers 2° latitude and 3° longitude. The simulation parallelograms are shifted north from the observation counterparts because the simulated squall line is shifted north from the one observed. This method includes a large number of samples for analysis, while excluding contamination from light precipitation ahead of the convective line as much as possible.

4.2. Criteria for Identifying Stratiform Precipitation Grid Points and Columns

Since conventional convective-stratiform separation methods based on radar reflectivity (e.g., Steiner et al., 1995) are not necessarily well suited for potentially biased simulated radar reflectivity, we instead use a surface rain rate threshold to identify *stratiform* precipitation columns within the analysis parallelograms. There are two kinds of observational precipitation rate data at different time scales. For the hourly scale rain rate (i.e., the hourly accumulated rainfall) comparison over a broad area, a threshold of 1–10 mm/hr is used for both simulations and observational retrievals (Figure 2). To reduce uncertainty in the evaluation, the lower threshold is set to 1 mm/hr due to poor performance of observational precipitation products at light rain rates (e.g., Ryzhkov et al., 2005). To distinguish the rain rates at the two different time scales, the hourly scale rain rate is referred to as HSRR for simplicity. Note that HSRR is not calculated with a moving coordinate since it is difficult to effectively identify the gust front of observed squall line from the observations because MESONET data are either not dense enough or only have limited spatial coverage. Therefore, there might be some uncertainty in the probability density function (PDF) of HSRR due to accumulation over 1 hr from different areas relative to different propagation speeds of the squall lines.

The other rain rate data are from disdrometer and VPR observations at 1-min time scale. Given an ~15 m/s system propagation speed, the horizontal resolution of these data is ~900 m. Therefore, 5-min WRF-outputted surface instantaneous rain rates on a 1-km grid are used for comparisons to these data. Both the spatial distribution and a cross section of Q2 and simulated instantaneous rain rates (Figures S1 and S2 in the supporting information) show that the surface instantaneous rain rates in the trailing stratiform region are generally less than 15 mm/hr but can exceed 10 mm/hr, especially for MY2 and P3, while convective rain rates generally exceed 15 mm/hr. Therefore, a threshold of 1–15 mm/hr is used as the criteria for exploring the model variability of instantaneous stratiform precipitation properties among the simulations

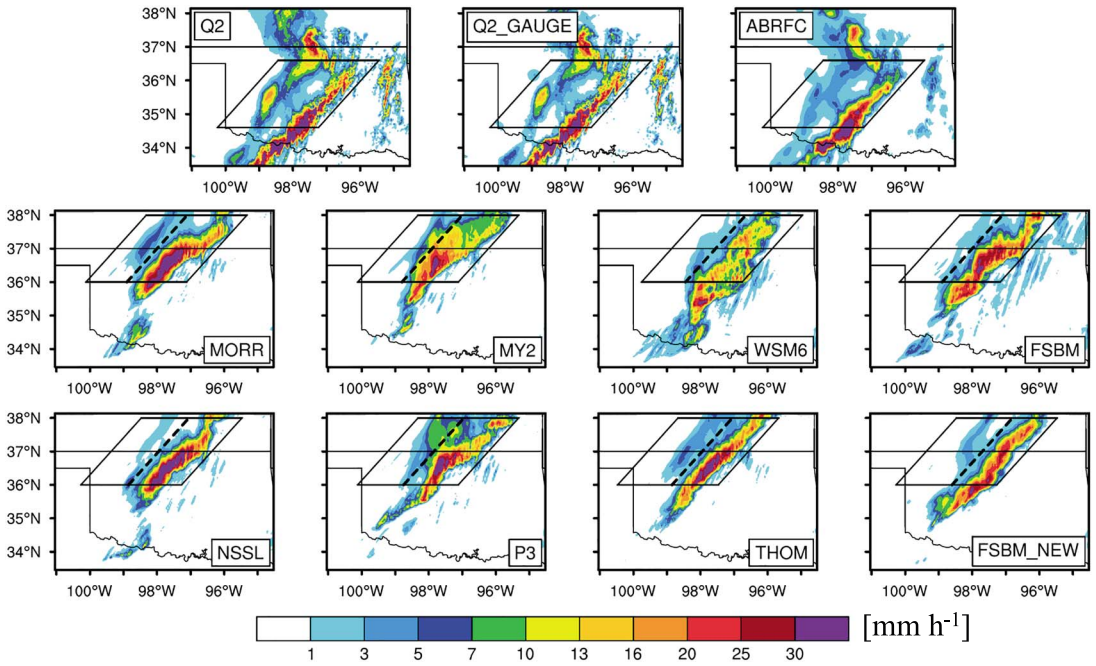

Figure 2. Spatial distribution of hourly precipitation from 1100 to 1200 UTC for three observational retrievals and from 1000 to 1100 UTC for simulations. The observation data sets are NEXRAD Q2, a bias-corrected NEXRAD Q2 (denoted by *Q2_GAUGE*), and Arkansas-Red Basin River Forecast Center (ABRFC) precipitation product. Observations and simulations are regridded to 0.04° × 0.04° mesh grids. The parallelograms denote the analysis region and are set to follow the movement of the observed and simulated system during the analysis time period. The dashed black line is used as an example to represent the boundary that approximately separates convective and stratiform precipitation regions for simulations. The simulated convective detrainment flux of total condensate is calculated based on this surface boundary.

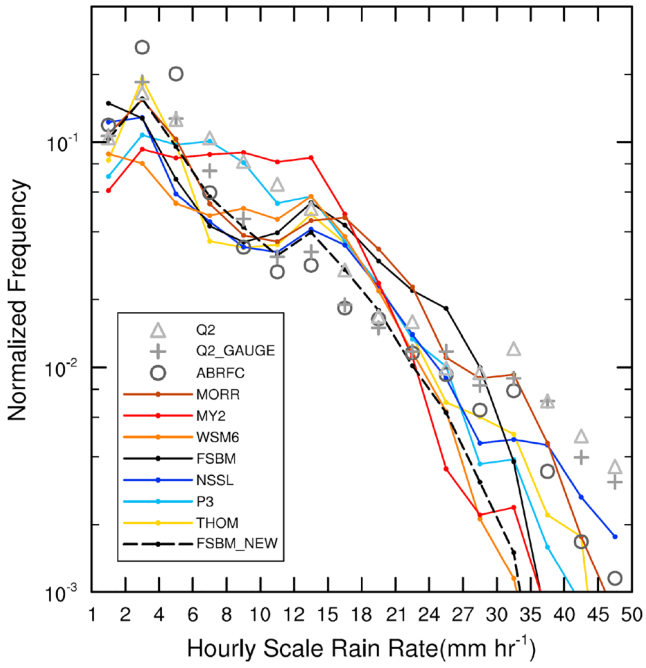

Figure 3. Normalized frequency of hourly precipitation during 1100–1400 UTC (Q2, Q2_GAUGE, and ABRFC observations) and 1000–1300 UTC (simulations). Observations and simulations are regridded to 0.04° × 0.04°mesh grids before calculation. The sample number of each rain rate bin is divided by the total grid points over the black parallelograms as shown in Figure 2.

with different microphysical schemes, where WRF output data at a 5-min interval are used for robust comparisons.

5. Results

5.1. Stratiform Precipitation Model Biases

5.1.1. Surface Precipitation Properties

Figure 3 shows the PDF of HSRR within the black parallelograms including both convective and stratiform regions during the analysis time period. The majority of simulations overestimates 12–21 mm/hr rain rate frequencies and underestimate 30–50 mm/hr rain rate frequencies. Most of the simulations significantly underestimate frequencies of moderate stratiform HSRR (2–6 mm/hr), which are the most frequent rain rates observed in the stratiform region. The underestimation ranges from 19% (THOM) to 62% (WSM6) compared to the value averaged from the three observational products. Differences between simulations and Q2_GAUGE/ABRFC products for heavy stratiform HSRR (6–10 mm/hr) frequencies are relatively small, with an exception of MY2 and P3 that have frequencies that are closer to the Q2 product. FSBM_NEW has much lower frequencies of heavy convective rainfall than FSBM. However, FSBM_NEW produces a greater frequency of stratiform HSRRs than FSBM between 2 and 10 mm/hr in Figure 3. FSBM_NEW has an improved MCS precipitation structure relative to observed with a distinct transition zone between the convective and stratiform regions and stratiform radar reflectivity magnitude that are both closer to observed relative to FSBM (Figures S1 and S2). Note that simulated Rayleigh radar

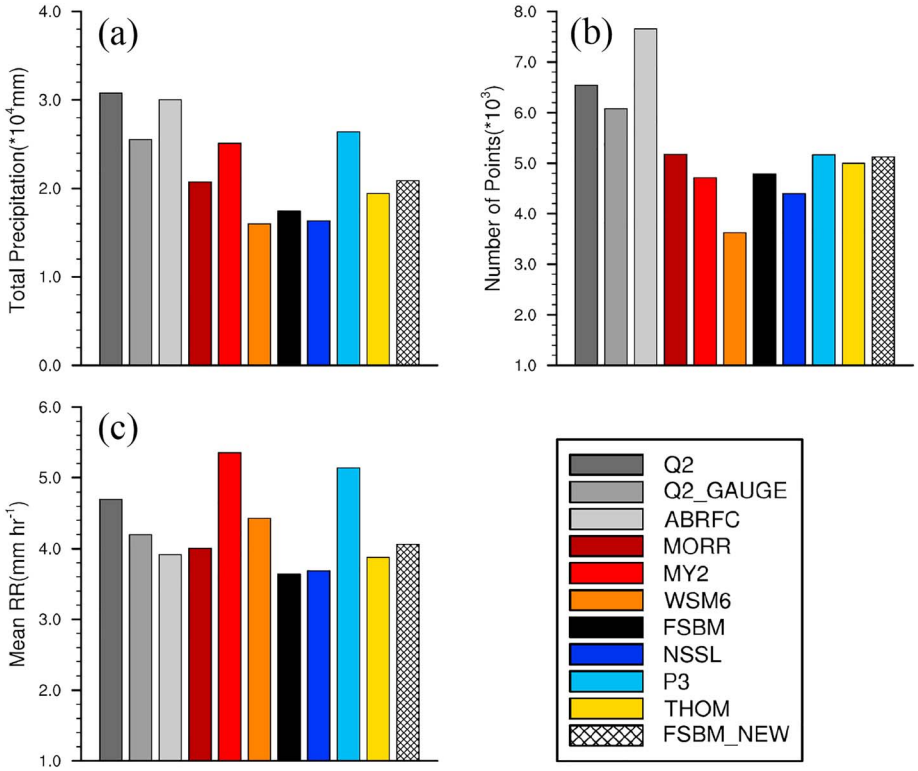

Figure 4. Stratiform rain properties include (a) total stratiform precipitation, (b) number of stratiform grid points, and (c) mean stratiform precipitation rate for the grid points with hourly scale precipitation rates of 1–10 mm/hr in the black parallelograms shown in Figure 2. The analysis time period is 1100–1400 UTC for observations and 1000–1300 UTC for simulations.

reflectivity is calculated using assumed hydrometeor properties in each microphysics scheme, and a simulated bright band parameterization is not included.

Differences between simulated and observed stratiform rainfall are further quantified in Figure 4. Most microphysics schemes underestimate total stratiform precipitation amount with MY2 and P3 as exceptions (Figure 4a). The total stratiform precipitation from MY2 and P3 is comparable to observations because of relatively high frequencies of heavy stratiform HSRR as shown in Figure 3. Stratiform precipitation area is consistently underestimated in all simulations (Figure 4b), particularly for WSM6, which only produces about half of the observed area. MORR, THOM, P3, and FSBM_NEW have values closer to the observed but still underestimate the area by more than 15% when compared to Q2_GAUGE and more than 30% when compared to ABRFC. Considering that mean stratiform HSRR produced by most simulations is comparable to or larger than observations (Figure 4c), model underestimation of the total stratiform precipitation clearly results from low-biased stratiform rain area. Note that P3, in which ice particle evolution is predicted, predicts both relatively large stratiform precipitation area and mean precipitation rate such that it produces total stratiform rainfall closest to observed.

We also performed analysis with another surface rain rate-based convective-stratiform partitioning method described in Churchill and Houze (1984; referred to as CH84). It is shown that the CH84 method with a 10 mm/hr (hourly scale rain rate) threshold gives very similar results as Figure 4. Further increasing the threshold to 15 mm/hr makes the underestimation of total stratiform precipitation and stratiform precipitation area smaller in most of the simulations. But differences across the microphysics schemes are still consistent. Therefore, the magnitudes of low bias in simulated total stratiform precipitation and stratiform precipitation area may be sensitive to the rain rate threshold used for analysis.

5.1.2. Rain Microphysical Properties

Figure 5 shows PDFs of simulated surface instantaneous rain rate at a 5-min interval compared with 1-min ground-based disdrometer and profiler observations collected at or near the SGP site during the

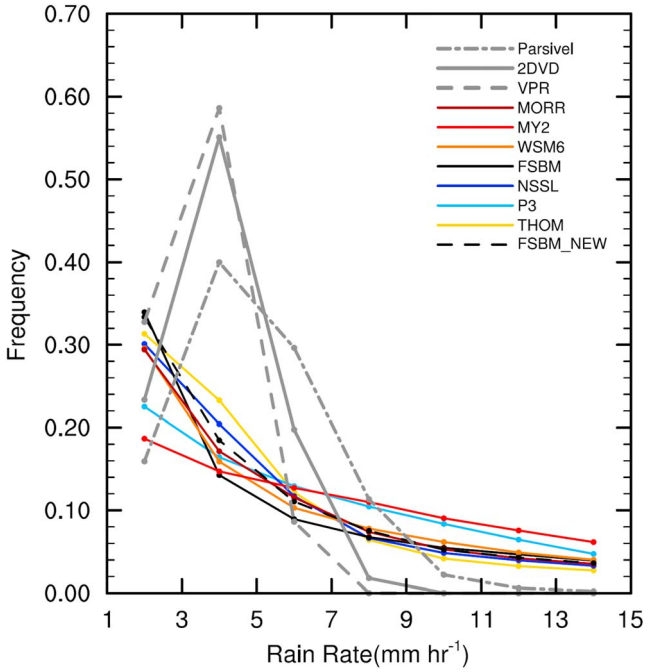

Figure 5. Probability density function (PDF) of surface rain rates from the ground-based observations and the simulations. The analysis time period is 1100–1400 UTC for observations and 1000–1300 UTC for simulations. The frequency is calculated from the sample number of each rain rate range divided by the total sample number of each simulation or observation. The analysis domains for simulations are the black parallelograms shown in Figure 2.

stratiform precipitation period. The differences between simulations and observations are generally consistent with those shown from Figure 3, whereby most schemes underestimate the frequencies of moderate stratiform rain rates (2–6 mm/hr). This indicates that the observations near the SGP site are fairly representative of the larger stratiform precipitation region. The results shown in Figure 5 do not change with the CH84 method discussed above.

The majority of the samples from the ground-based observations fall within the 1–7 mm/hr rain rate range. To exclude the influence of rain rate PDF differences between observations and simulations on stratiform properties, we conduct comparisons for limited rain rate ranges of 1–3, 3–5, and 5–7 mm/hr. Figure 6 shows RSD comparisons for these three ranges. The disdrometer measurements are not robust for raindrop diameters smaller than ~0.5 mm, so disdrometer data below this threshold are discarded in the comparison. The calculation of RSDs for the simulations is included in the supporting iformation (SI). As shown in Figure 6, RSDs observed by the 2DVD and Parsivel disdrometers agree with each other quite well for the 1–3 mm/hr rain rate range, while differences become larger as rain rate range increases, especially for raindrops larger than 2.5 mm in diameter. Note that 2DVD data are only from one location, which may not be as representative as the greater samples from Parsivel disdrometer data in this case. However, the difference could also result from the measurement uncertainty between the Parsivel and 2DVD. For example, the Parsivel disdrometer tends to underestimate the concentration of small raindrops while overestimating the concentration of large ones (Tokay et al., 2013), something that may be happening in this case (Figure 6). On the other hand, the RSD differences between observations and simulations are generally consistent across the different stratiform rain rate ranges. The majority of schemes tend to overestimate raindrop concentrations between 0.5 and 1.0 mm diameters. For large raindrop (>3.0-mm) concentrations, simulations perform worst for the 1–3 mm/hr range but reproduce observations fairly well for the higher rain rate ranges. WSM6 and FSBM are the exceptions, having a low bias in large raindrop concentration for all three rain rate ranges. However, FSBM_NEW is able to reproduce the large raindrop concentrations observed by the 2DVD, performing better than FSBM (Figure 6). This difference is revisited in section 5.2. MORR and THOM generally have more large raindrops than the other schemes, which is investigated in further detail below.

By utilizing vertical profiles of stratiform rain properties from VPR retrievals, we can compare the evolution of simulated and observed rain properties as raindrops approach the surface. Profiles of observed and simulated stratiform radar reflectivity, Doppler velocity, mass-weighted mean diameter (D_m), and RWC for the 1–3 mm/hr range are shown in Figures 7 and 8. Profiles for the other two rain rate ranges are shown in Figures S3–S6, and model biases are generally similar to those in 1–3 mm/hr range. Note that the calculations of Doppler velocity and D_m are detailed in the SI. The observed radar reflectivity and Doppler velocity decrease from ~3-km altitude to the surface by ~3 dBZ and 1 m/s, respectively (Figure 7). WSM6 and NSSL reproduce both observed profile shapes reasonably well, while FSBM, FSBM_NEW, and THOM generally reproduce the Doppler velocity slope. However, WSM6 and FSBM significantly underestimate the radar reflectivity and Doppler velocity at all altitudes, suggesting that the underestimation of large raindrops at the surface (Figure 6) is mainly caused by errors above the 3-km altitude. MORR produces incorrect vertical profile slopes (i.e., the increase of radar reflectivity and Doppler velocity moving toward the surface), suggesting that excessive size sorting is occurring, as highlighted in previous studies (e.g., Morrison et al., 2015; Varble et al., 2014b). Excessive size sorting is largely corrected in THOM through adjustment of the number-weighted fall speed toward the mass-weighted fall speed, but it overestimates the radar reflectivity and Doppler velocity by ~2 dBZ and ~2 m/s, respectively. Radar reflectivity magnitudes are best represented by THOM at 3-km altitude but are best predicted by MY2, NSSL, P3, and FSBM_NEW at 0.5-km altitude although the corresponding

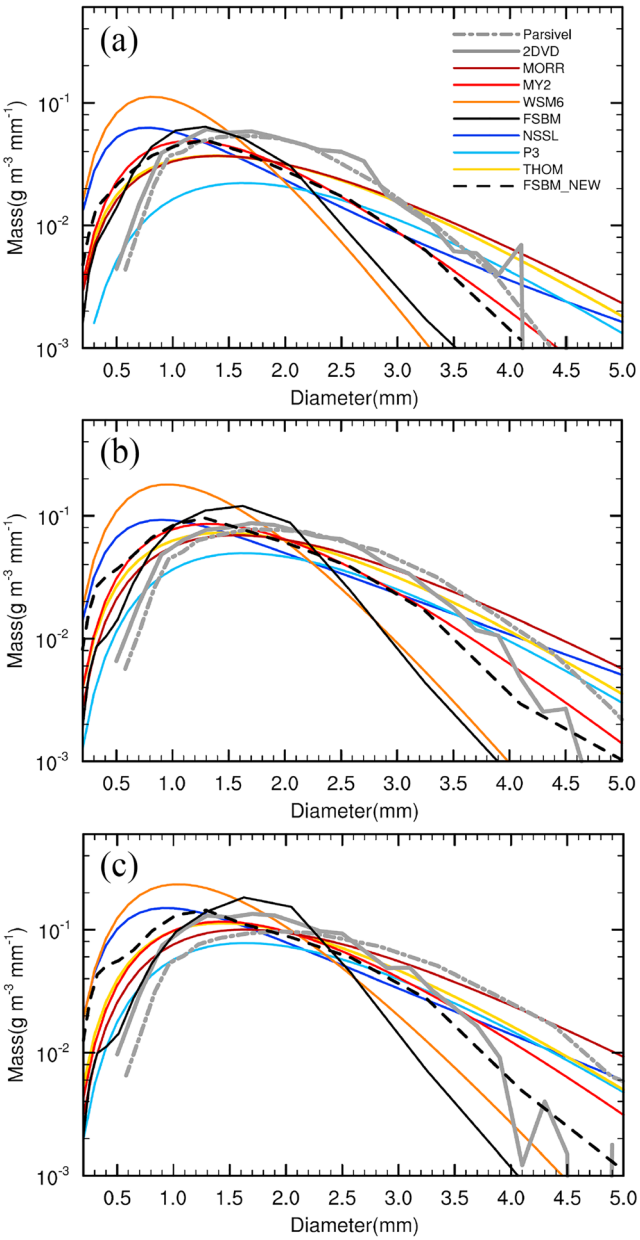

Figure 6. Surface rain mass size distributions from ground-based observations and the simulations for (a) 1–3-, (b) 3–5-, and (c) 5–7-mm/hr rain rate range, averaged over 1100–1400 UTC for observations and 1000–1300 UTC for simulations. The analysis domains for simulations are the black parallelograms shown in Figure 2. The rain size distribution (RSD) is multiplied by raindrop mass to obtain the mass size distributions. Detailed description about the calculation of simulated RSDs is included in the supporting information.

internal variabilities of NSSL and P3 are larger. The latter four schemes also generally capture observed Doppler velocity magnitudes. Note that the overestimations of radar reflectivity and Doppler velocity in THOM have been addressed by a modified Thompson scheme as shown in Brown et al. (2017).

The differences in retrieved and simulated D_m validate previous discussions about WSM6 and FSBM lacking large raindrops, while MORR and THOM produce too many large raindrops at lower levels (Figure 8a). All schemes except WSM6 underestimate RWC (Figure 8b) with the underestimation generally increasing with height. The underestimations of RWC by most schemes are reduced for the 3–5-mm/hr range (Figure S4). For the 5–7-mm/hr range, some schemes even produce RWCs that are closer to retrieved values below 2.0-km altitude (Figure S6). However, only WSM6 simulates greater RWC than retrieved values in all three rain rate ranges, which means that larger RWC is required for WSM6 to produce a similar surface rain rate as observed and is consistent with tropical MCS results in Varble et al. (2014b). Thus, even though both WSM6 and FSBM have too many small raindrops and too few large raindrops, the mean stratiform HSRR of WSM6 is larger than FSBM and all other simulations except MY2 and P3 (Figure 4c).

It is worth noting that the drastic reduction of retrieved RWC from the ~3-km altitude to 0.5-km altitude did not occur for the tropical MCS case shown in Varble et al. (2014b) where retrieved and simulated stratiform RWCs remain nearly constant with height. This is likely caused by much greater rain evaporation in this drier midlatitude continental environment as compared with the more humid tropical oceanic environment (e.g., Liu & Zipser, 2013). Additionally, this case has a well-organized rear inflow jet and mesoscale downdraft at midlevels in the stratiform region that could be adiabatically warming and drying the environment more than in the tropical MCS case studied in Varble et al. (2014b) where the VPR was not as well positioned to sample mesoscale downdrafts. The underestimation of the RWC reduction rate as raindrops approach the surface by all schemes except WSM6 may suggest that stratiform rain evaporation is greater in reality than in the simulations.

Greater rain evaporation is potentially caused by stronger descending motions. Observed downdraft motion is indeed much stronger than simulated, as shown in Figure 9 where joint PDFs between vertical velocity and RWC are plotted. Note that the dual-frequency VPR vertical velocities used in this study were validated against a separate collocated 915-MHz VPR at the SGP CF using a single-frequency VPR vertical velocity retrieval method (Giangrande et al., 2013). The single-frequency VPR method was validated by a multi-Doppler radar 3-D wind field retrieval at the SGP CF using several rain events during MC3E (North et al., 2017). The three observational data sets show similar mean profiles of vertical velocity (i.e., obvious downdraft motion) for rain rate ranges considered here. WSM6 has the greatest evaporation (see section 5.2) and produces the joint PDF closest to observed but significant differences remain. For other simulations, nearly half of the stratiform RWC is in the regions of rising motion, while the majority of observed RWC is in the regions of descending airflow. However, significant vertical differences exist; that is, at 3-km altitude the simulated RWC is mainly associated with the descending regions except that the range of RWC is underestimated. In contrast, simulations reproduce the range of RWC at 0.5-km altitude but underestimate the spread of vertical motion and more symmetrically distribute RWC between the rising and descending

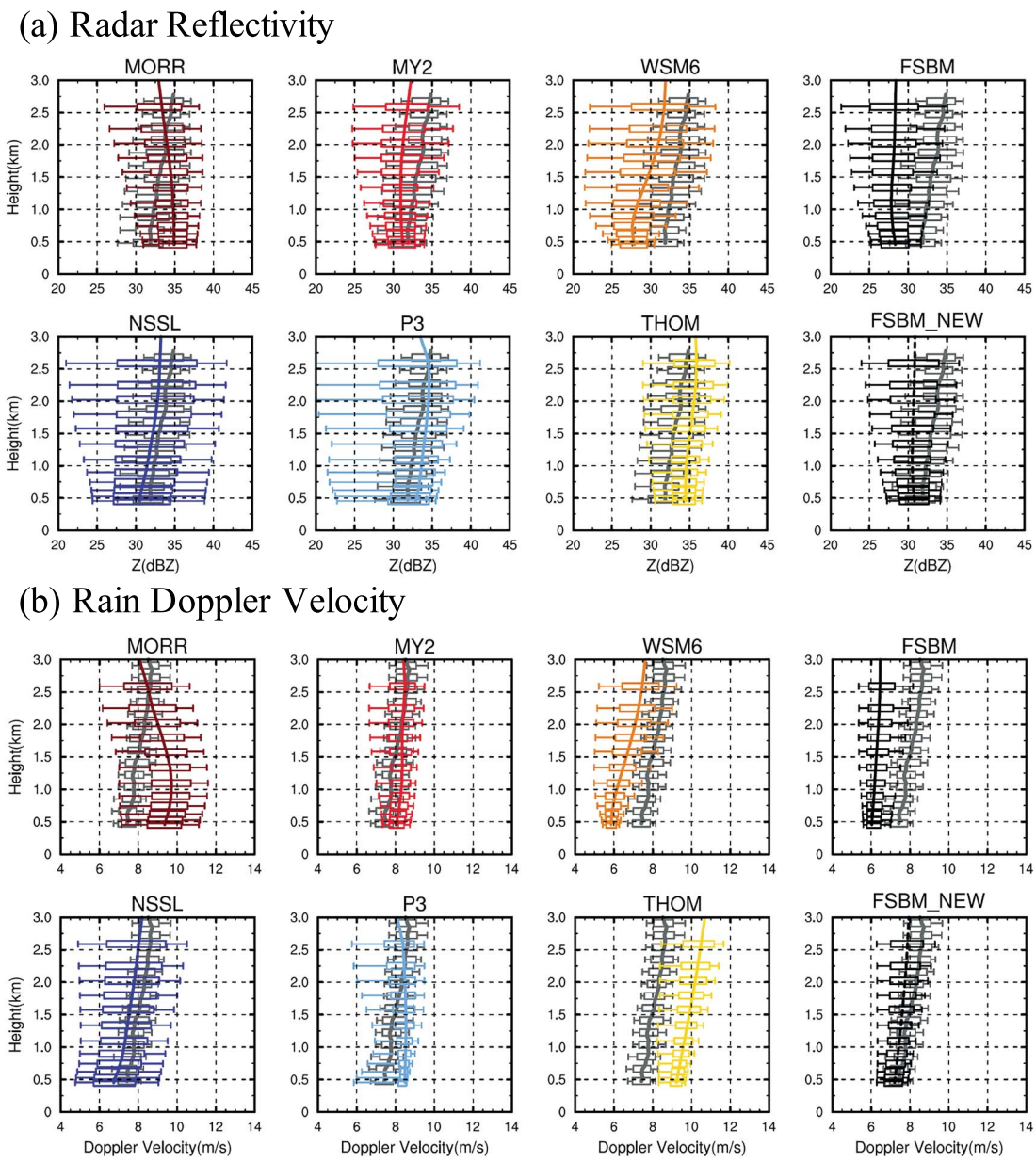

Figure 7. Profiles of (a) radar reflectivity and (b) rain Doppler velocity over columns with 1–3-mm/hr surface rain rate, averaged over 1100–1400 UTC for observation and 1000–1300 UTC for simulations. The analysis domains for simulations are the black parallelograms shown in Figure 2. The gray line represents the median profile from vertically pointing radar (VPR) data. The colored lines represent the median profiles for simulations. The 25th and 75th percentiles are represented by boxes, while the 10th and 90th percentiles are represented by whiskers at each layer for both VPR data and simulations.

motions (Figure S7). These features consistently exist for all stratiform rain rate ranges with little sensitivity to the microphysics or planetary boundary layer schemes used in the simulations.

These model-retrieval differences may be related to a bias in the altitude and descent of the rear inflow jet. In reality, the rear inflow jet descends slowly from the melting level to lower altitudes through the stratiform region, whereas the simulated rear inflow jets generally descend more quickly over a smaller region toward the back of the stratiform precipitation. This is highlighted by the relatively broad observed zonal wind peak (i.e., width of the peak) at ~3-km altitude and relatively narrow simulated zonal wind peaks between 1.5- and 2.5-km altitudes (Figure 10b). The simulated rear inflow jet being at lower altitudes than observed may limit the potential strength of the mesoscale downdraft between 1- and 3-km altitudes (Figure 10a). Weaker descending motion may result in less rain evaporation, as indicated by the lower than observed

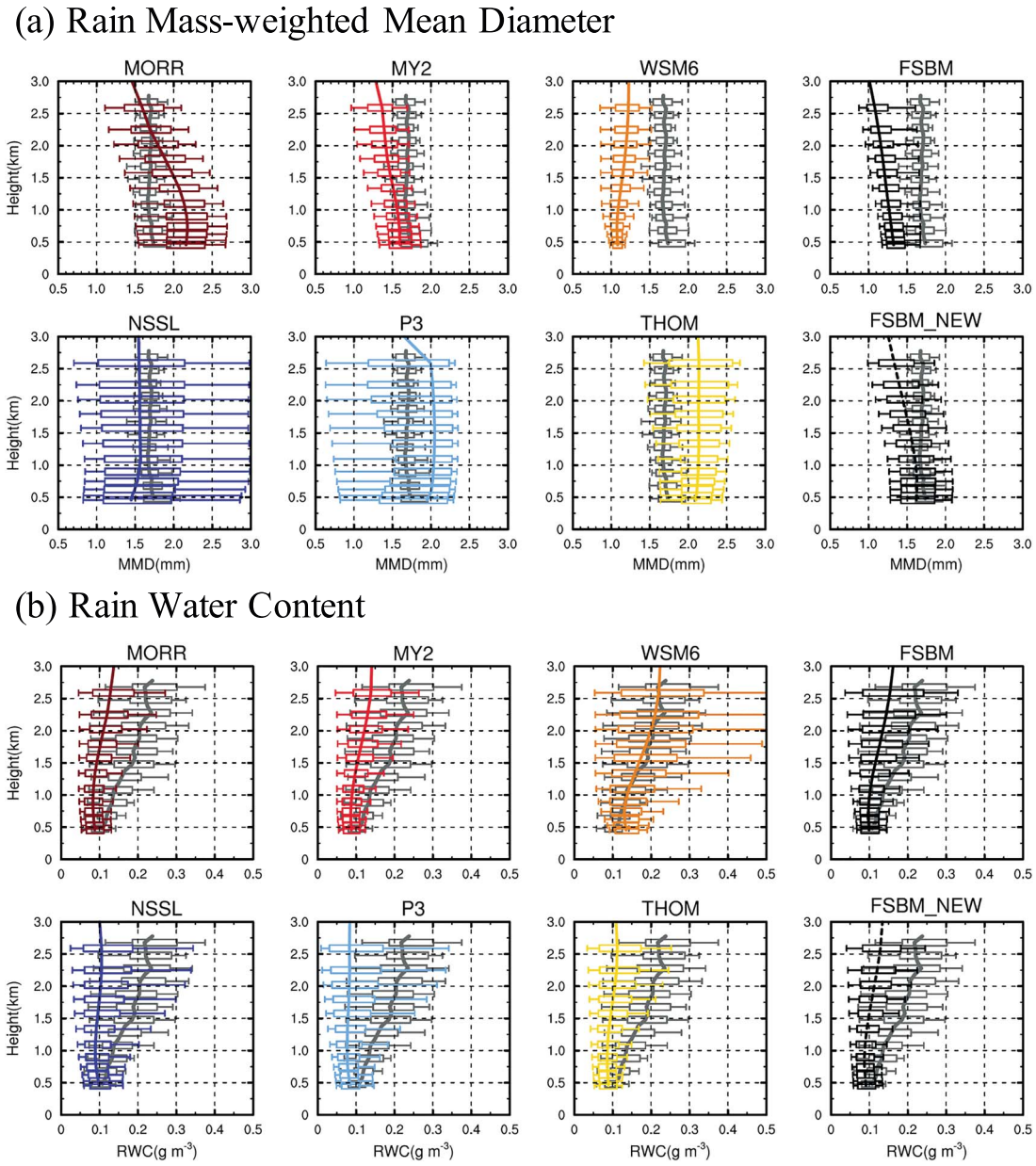

Figure 8. Same as Figure 7, except for profiles of (a) rain mass-weighted mean diameter and (b) rainwater content.

decrease of RWC between 3- and 0.5-km altitudes in the simulations (Figure 8b). Although a stronger downdraft should produce more warming and drying with all else equal, greater evaporation would at least partially compensate this effect. Indeed, the relative humidity profiles retrieved by the Raman lidar and radiosondes are similar to those simulated, with the exceptions of WSM6 and MY2 in which air is cooler and moister below 2-km altitude (Figure 11). This suggests that potentially greater evaporation in the observed case is not caused by lower relative humidity than simulated, which supports the hypothesis that the rear inflow jet and mesoscale downdraft are involved in the model-observations differences. Analyses for the other two greater rain rate ranges generally show similar results in terms of simulation-retrieval and intersimulation differences (Figures S8–S10).

5.1.3. Ice Microphysical Properties

Above the melting level (~4-km altitude), the in situ aircraft measurements and NEXRAD retrievals are used to evaluate simulated stratiform ice properties. The first aircraft track (i.e., 1335–1420 UTC) over the

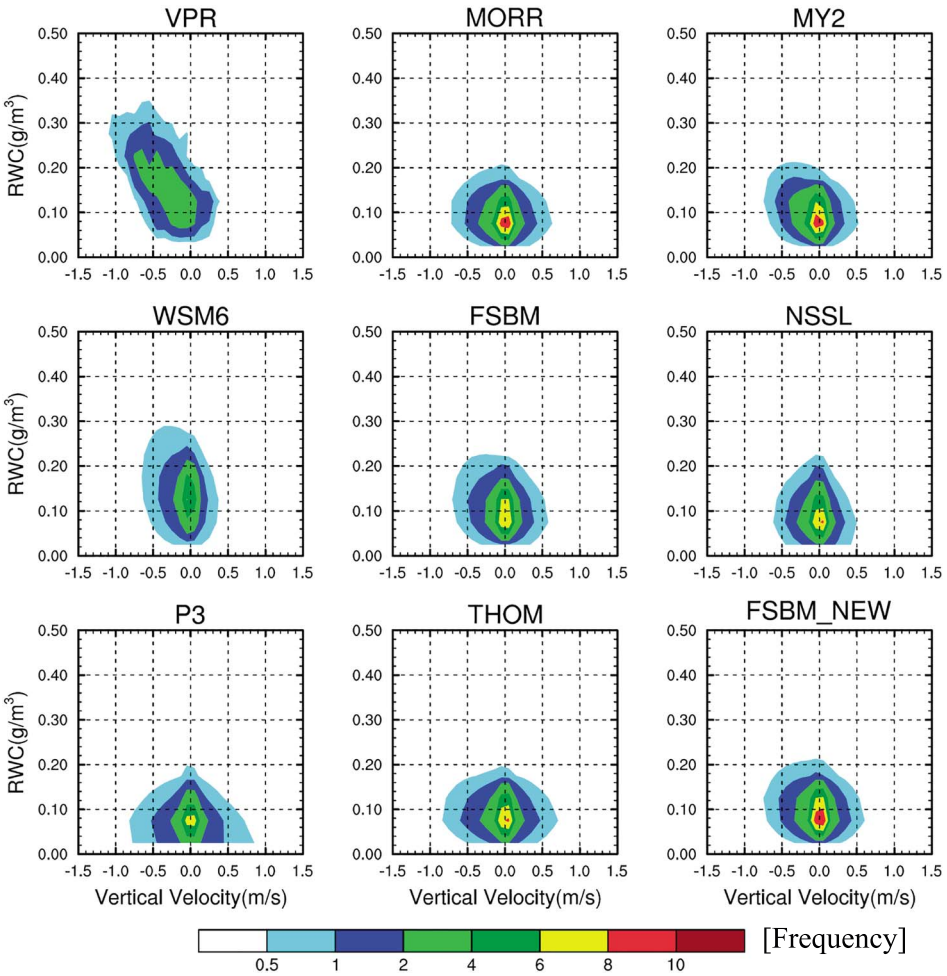

Figure 9. Joint PDFs of rainwater content (RWC) and vertical velocity between 0.5- and 3-km altitudes. The columns in the Figure 2 black parallelograms with 1–3 mm/hr surface rain rate are used. The analysis time period is 1100–1400 UTC for observations and 1000–1300 UTC for simulations. The bin interval for calculation is 0.1 m/s for vertical velocity and 0.05 g/m^3 for RWC.

extensive ground-based instruments near the SGP site is chosen for evaluation. The observed surface rain rates during this period were mostly 1–3 mm/hr, and thus, this range is used for comparisons with aircraft measurements. Simulated IWC is the sum of the mass within all ice species categories. Aircraft-measured ice particle number size distribution is used to estimate mass size distribution and IWC by using the mass-size relationship mentioned in section 2.

As shown in Figure 12a, most simulations generally overestimate IWC above 7-km altitude compared to aircraft retrievals. The overestimation of IWC is largest for THOM and FSBM_NEW, while IWC produced by FSBM is close to those retrieved with aircraft observations. The other common model bias is that simulated stratiform IWCs tend to decrease below 5-km altitude, while they increase toward the melting level in aircraft data. As a result, simulations consistently underestimate IWC directly above the melting level, which likely contributes to the underestimation of RWC below 3-km altitude. WSM6 is the only scheme that does not experience a decrease of IWC below 5-km altitude such that it has more IWC at and right above the melting level compared with other schemes, which is consistent with the relatively larger RWC below the melting level. The overestimation of IWC above 7-km altitude may be caused by detrainment that is too high because of overestimated convective intensity shown in Part I (Fan et al., 2017). The underestimation of IWC just above the melting level may also be related to convective updrafts that are too intense in simulations. For example, detrainment of condensate too high in the troposphere can lead to excessive sublimation of ice particles before they reach the melting level as they fall through subsaturated air. In reality, convection

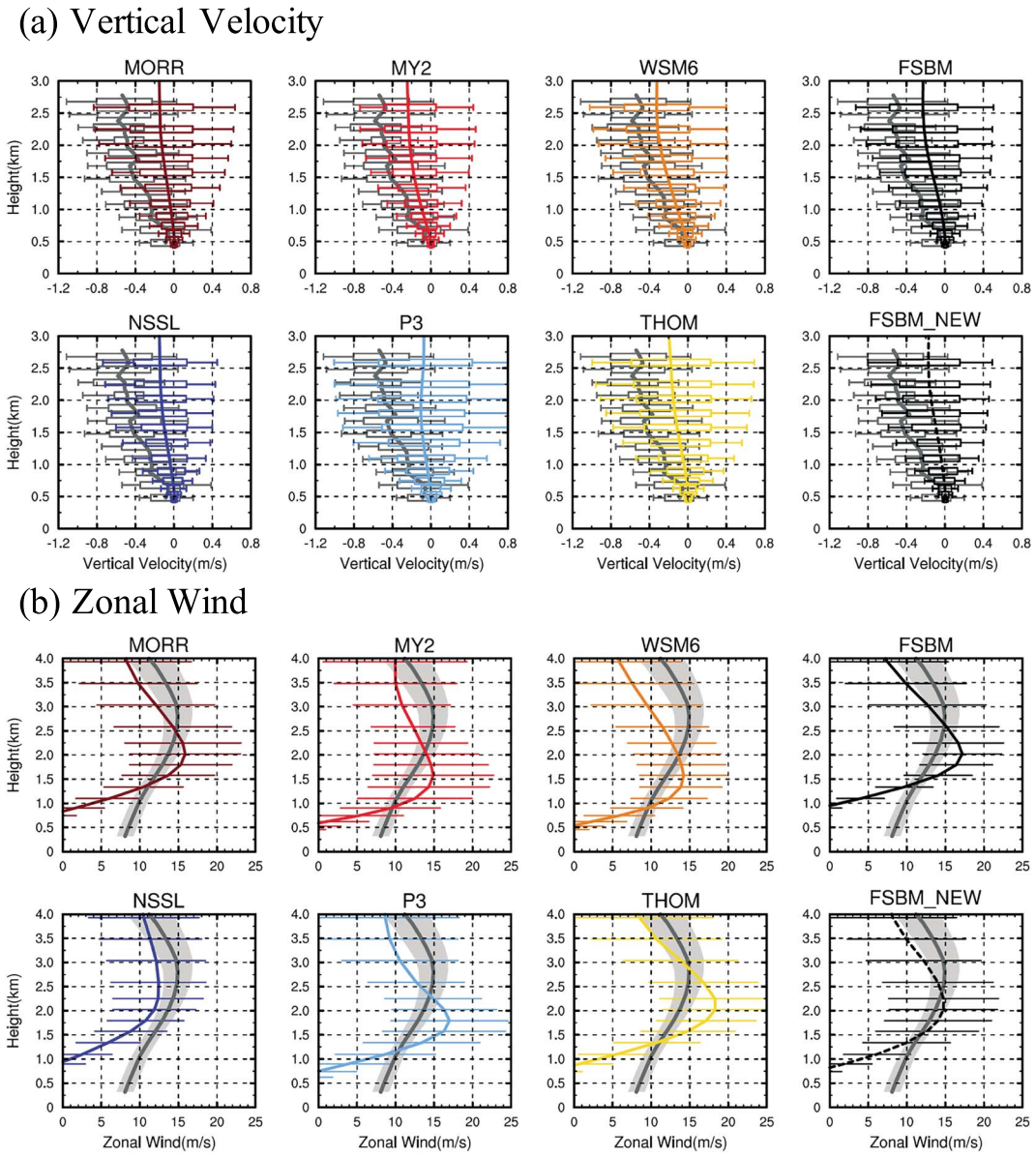

Figure 10. Profiles of (a) vertical velocity and (b) zonal wind over columns with 1–3 mm/hr surface rain rate, averaged over 1100–1400 UTC for observation/retrieval and 1000–1300 UTC for simulations. The analysis domains for simulations are the black parallelograms shown in Figure 2. For (a), the definition of lines, boxes, and whiskers follow Figure 7. The observed vertical velocity data are from VPR. For (b), the temporal mean profiles and standard deviations are shown due to limited samples to calculate percentiles robustly for the retrievals. The gray line represents the temporal mean profile, and the gray filled area represents standard deviation for retrieved zonal wind. For simulations, the mean profiles and standard deviations are represented by the colored lines and bars, respectively. Zonal wind data at the SGP CF are obtained from a multi-Doppler radar retrieval and matched to the VPR rain rate at the nearest time.

may be weaker with greater detrainment of condensate, water vapor, and buoyancy at lower altitudes (e.g., 3–7 km), which would support greater deposition and lead to a potential increase of IWC approaching the melting level.

Comparing WRF results with the NEXRAD IWC retrievals over the broader stratiform region and longer time period, consistent results emerge in that the IWC is overestimated above 7-km altitude by the majority of simulations (Figure 12b). Further examination of ice particle size distributions at two altitudes (~5.8 and 6.7 km) that were sampled extensively by the aircraft shows that most schemes agree well with observed ice number concentrations of particles larger than 2 mm in diameter at 6.7-km altitude (Figure 13a). However,

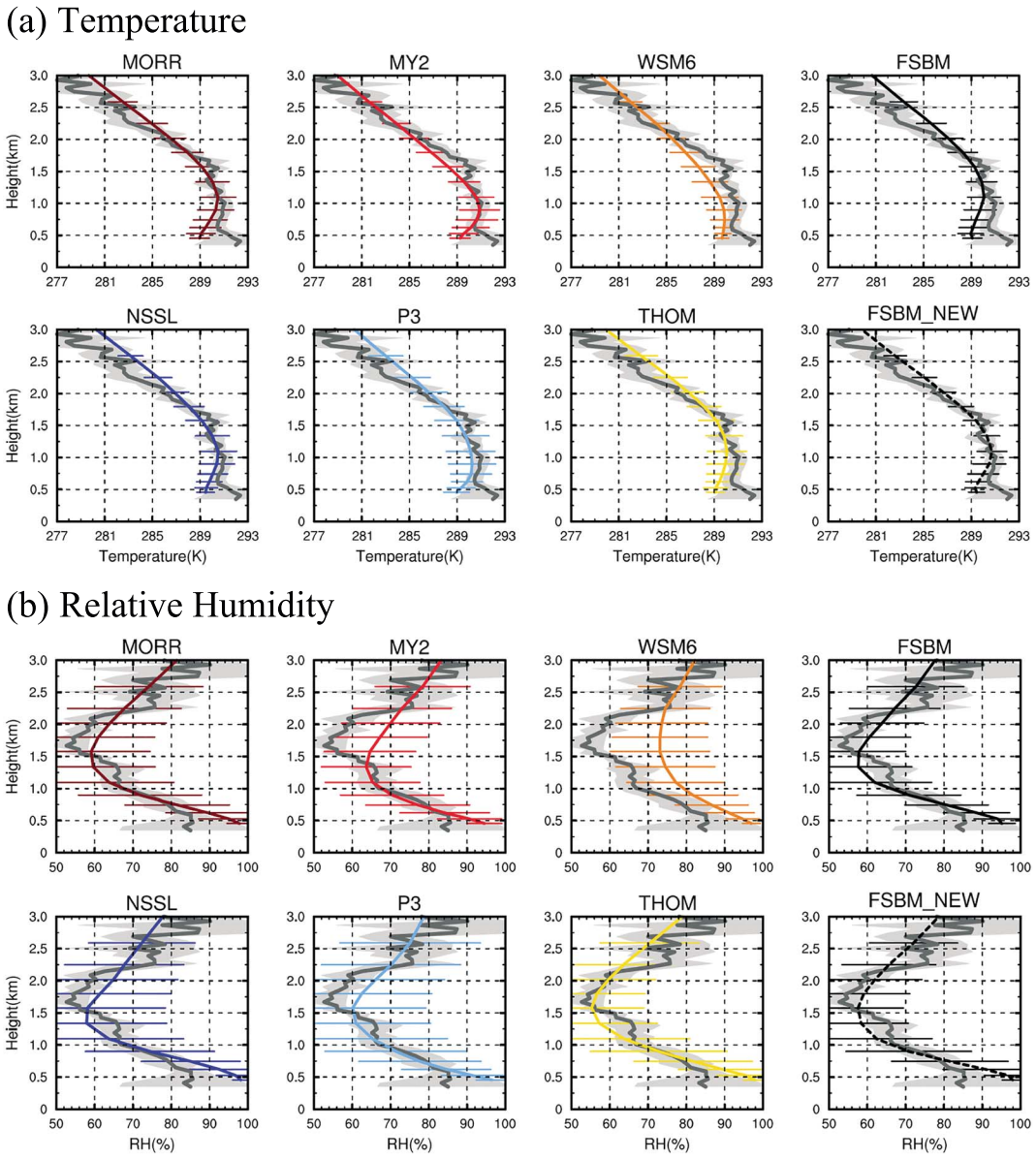

Figure 11. Same as Figure 10, except for profiles of (a) temperature and (b) relative humidity. The temporal mean profiles and standard deviations are shown due to limited samples to calculate percentiles robustly for retrievals. Temperature and relative humidity data are retrieved by a Raman lidar with 10-min resolution and are matched to the nearest VPR rain rate in time.

simulations tend to underestimate the number concentrations of 0.2–2-mm diameter ice particles and the underestimation increases moving from the 6.7 to 5.8-km altitude (Figures 13a and 13c). Simulated ice mass size distributions show a general low bias in mass for particles with diameters of 0.1–1 mm. Most schemes distribute more mass to ice particle with diameters larger than 2 mm than retrieved by aircraft measurement (Figures 13b and 13d). FSBM has a clearly low bias in ice mass over the diameter range larger than 1 mm at 5.8-km altitude despite agreement at 6.7-km altitude, which may explain the lack of large raindrops in FSBM in Figure 6. THOM and FSBM_NEW are the only two schemes that produce mass in the 0.3–1-mm diameter range that is similar to observed but FSBM_NEW places too much mass in diameters >1 mm and THOM places too much mass in diameters <0.3 mm and in 1–4-mm diameter range, which is consistent with the large overestimation of IWC by those two schemes shown in Figure 12a. The greater number of ice particles at diameters >2 mm in FSBM_NEW as compared to FSBM (Figure 13c) leads to its better performance in reproducing large raindrops at the surface (Figure 6).

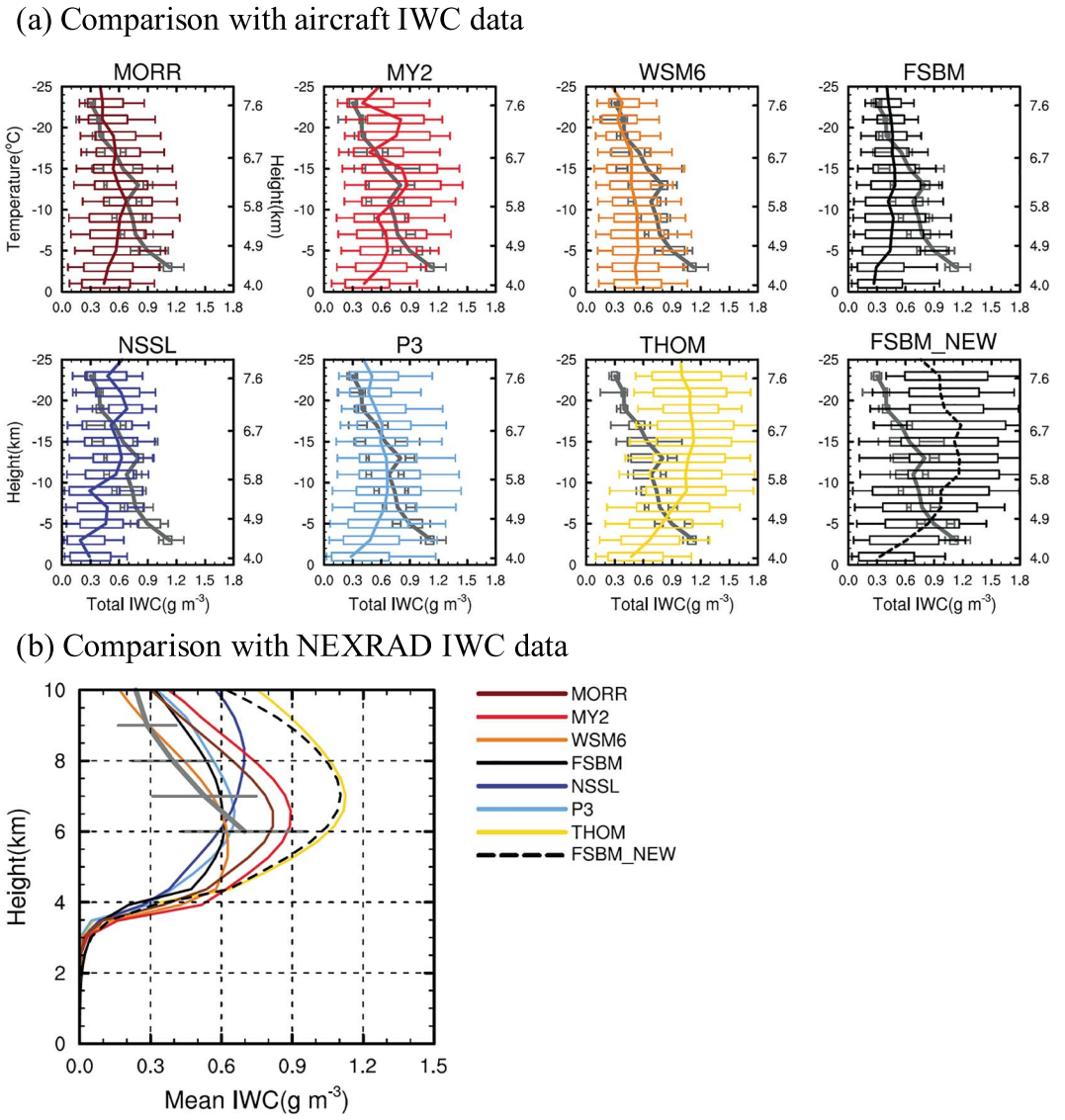

Figure 12. Vertical profiles of total ice water content (IWC) compared with (a) aircraft best estimated data and (b) NEXRAD-retrieved data. For (a), the definition of lines, boxes, and whiskers follow Figure 7. The analysis time period for (a) is 1335–1420 UTC for observations and 1235–1320 UTC for simulations. The aircraft data are binned every 2° in temperature. For (b), the gray line and colored line represent temporal mean profiles for retrieval and simulations, respectively. The gray bars represent the standard deviations for the retrievals. The analysis domain and time period for (b) is the same as Figure 4 but for the columns with 1–3-mm/hr surface rain rate to be consistent with the aircraft best estimated IWCs.

It was previously shown that 3-km altitude RWC and 4.5-km altitude IWC are underestimated by simulations. The distributions in Figure 13 show that these underestimations are generally the result of low-biased ice particle number concentration and mass over the 0.2–2-mm diameter range. Comparing 5.8- to 6.7-km altitude size distributions shows that observed ice evolves differently than simulated ice as it falls. Observations show a clear increase in the number and mass of large particles moving from 6.7 to 5.8 km, while changes in the number and mass of small particles are limited. This indicates that ice is aggregating but the replenishment of small particles also indicates growth through deposition, consistent with the increase in IWC. Simulations experience slight increases in the number and mass of relatively large ice particles (>2 mm in diameter) and slight decreases in the number and mass of relatively small ice particles (0.2–1 mm in diameter), suggesting weaker aggregation compared with observations. The difference in the observed and simulated IWC profiles may be caused by a combination of

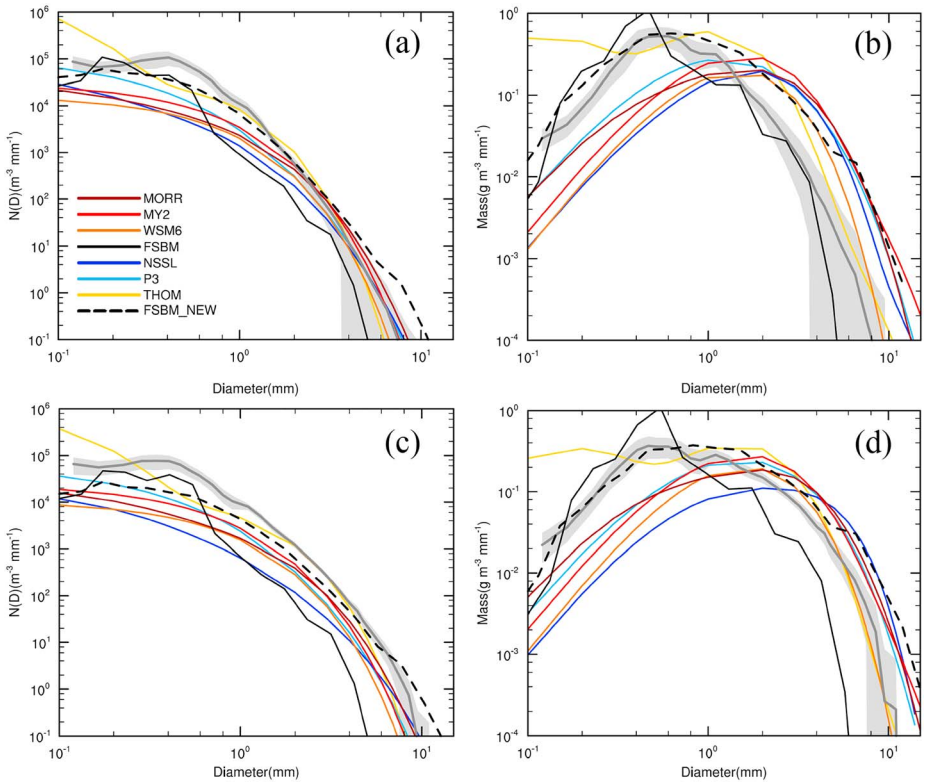

Figure 13. Mean ice particle size distributions (PSDs) at (a) 6.7-km altitude and (c) 5.8-km altitude. (b) and (d) are the corresponding mean ice mass size distributions (MSDs) at these two altitudes. The aircraft sampled precipitating stratiform clouds around these two altitudes extensively. The gray solid line represents mean aircraft in situ measurements, and the standard deviation is represented by the gray filled area. Simulated ice PSDs sum contributions from all ice species. Because snow and hail bins in FSBM and FSBM_NEW have different diameters, the hail PSD is added to the nearest snow PSD bin for simplicity. The ice MSD is calculated by multiplying the PSD by the mass-diameter relationship for each ice species and adding the contribution from each species together. The sampled areas for simulations are the columns in the Figure 2 black parallelograms with 1–3-mm/hr surface rain rate. The analysis time period is 1335–1420 UTC for observation and 1235–1320 UTC for simulations.

simulated deposition that is too weak and sedimentation that is too fast, but untangling these two factors requires further information.

5.2. Causes for Model Spread

The stratiform precipitation properties shown in Figure 4 vary by about a factor of 1.5, which is generally similar to the spread in convective intensity and precipitation that vary by a factor of about 1.5 in Part I. The large spread in surface mean stratiform HSRR across the microphysics schemes (Figure 4c) is generally consistent with that of rain downward mass flux shown in Figure 14a. MY2 and P3 produce the largest rain mass fluxes because both RWC and rain mean fall speed are relatively large (Figures 14c and 14e). FSBM has the smallest rain mass flux, resulting from relatively small rain mean fall speed rather than low RWC. Although rain mass flux and RWC produced by WSM6 are as large as those from MY2 and P3, the surface rain rate is much smaller than MY2 and P3 because of the smaller rain mean fall speed at lower levels, which is caused by too many small raindrops and a lack of large raindrops (Figure 6). Additionally, WSM6 has the largest evaporation rate, which further contributes to the rapid decrease in rain mass flux from 3-km altitude to the surface (Figure 15c). Overall, the spread of rain mass fluxes across the simulations depends on both the variability of rain mean fall speed and RWC. The spread in rain mass-weighted mean fall speeds is primarily caused by differences in RSDs rather than differences in assumed terminal velocity-size relationships between the different microphysics schemes (Figure 16).

The initial stratiform RWC around 3-km altitude is primarily produced by melting of ice particles, and the melting rate across simulations varies by a factor of 2 (Figure 15a). The contribution of autoconversion

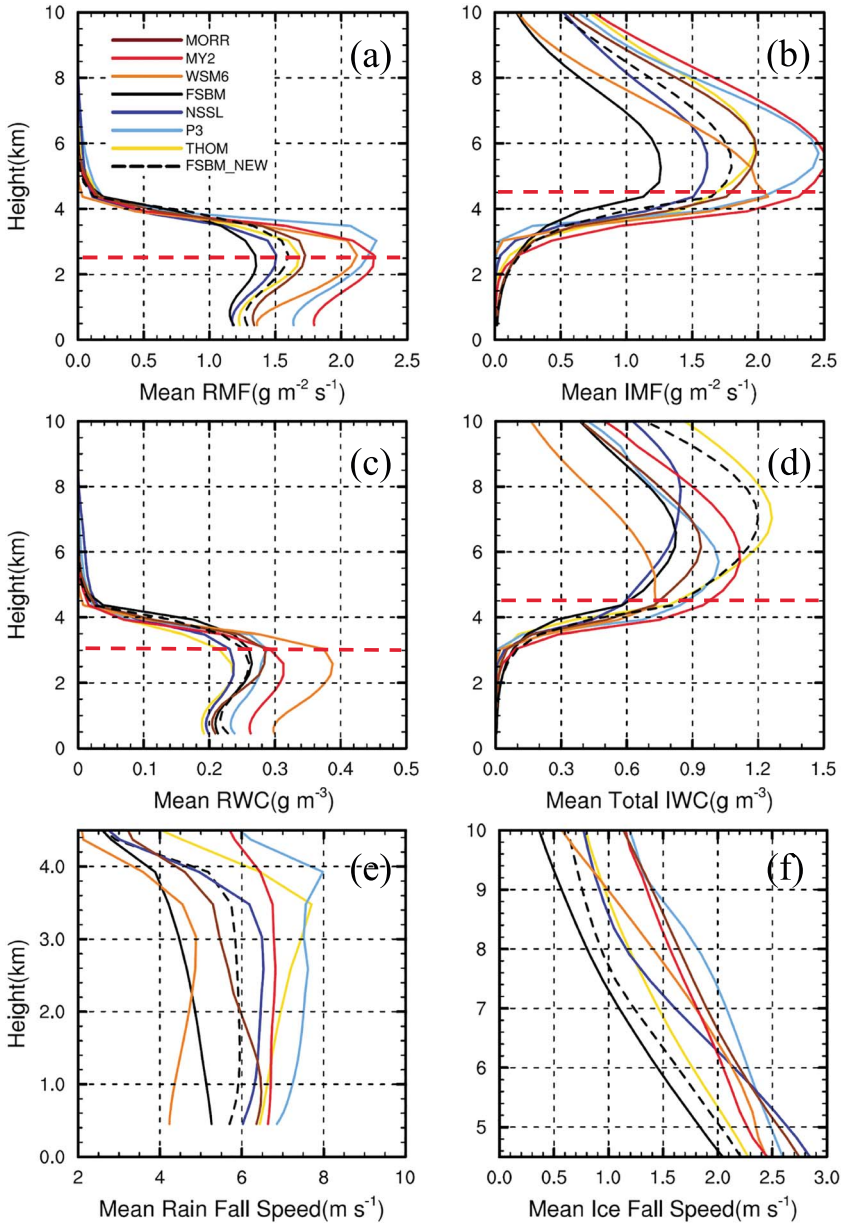

Figure 14. Mean profiles of (a) downward rain mass flux, (b) total downward ice mass flux, (c) rainwater content, (d) total ice water content, (e) rain mass-weighted mean fall speed, and (f) ice particle mass-weighted mean fall speed, averaged over columns with surface instantaneous rain rate of 1–15 mm/hr in the Figure 2 black parallelograms using 5-min frequency data. The analysis time period is 1000–1300 UTC. The red dashed line represents the layer that is just above or below the melting level.

and collection of droplets by raindrops to RWC is very small in the stratiform region (Figure 15b) because of a scarcity of cloud droplets in predominantly subsaturated conditions (Figures 11b and S9). Below 2-km altitude, rain evaporation generally dominates the net budget of RWC, with rates varying by up to a factor of 2 (Figure 15c).

Rain mass fluxes at 3-km altitude (red dashed line in Figure 14a) clearly correspond with rain mass fluxes at the surface, but they also clearly correspond well to the total downward ice mass fluxes right above the melting level (red dashed line in Figure 14b). Therefore, the model variability in surface rain rates is likely primarily a result of the variability in ice downward mass fluxes right above the melting level. Similar to rain mass fluxes, the ice mass flux variability depends on both IWC and ice mass-weighted

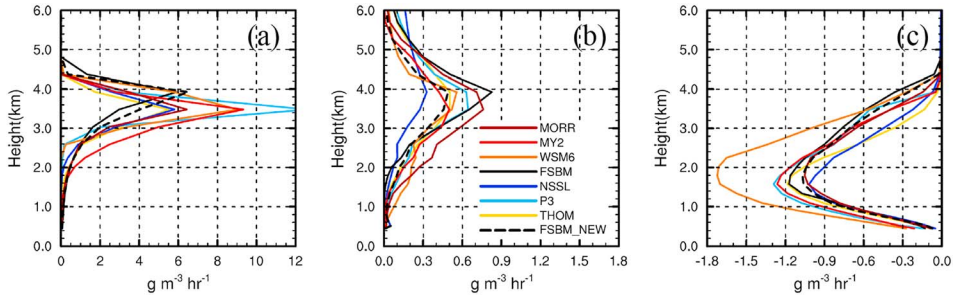

Figure 15. Mean profiles of microphysical process rates for (a) melting, (b) collection and autoconversion, and (c) evaporation. Collection and autoconversion refer to rain collecting cloud water and the autoconversion of cloud water to rainwater. Note that (a) has a much larger *x* axis range than (b) and (c). The data are processed in the same way as Figure 14.

mean fall speed variability, which both depend on the dominant ice species and the properties (e.g., number and mass size distributions) for each species in the simulations (Figure 17).

Ice particle fall speed plays an important role in modulating ice downward mass flux. For example, THOM and FSBM_NEW have the largest IWCs among all simulations (Figure 14d), but the ice vertical mass fluxes are intermediate (Figure 14b) because of relatively slow ice particle mass-weighted mean fall speeds (Figure 14f). The slow ice particle mass-weighted mean fall speeds in THOM and FSBM_NEW are caused by the dominant hydrometeor type being slow-falling small snow particles (Figures 17b and 17e). For the schemes with the largest ice vertical mass fluxes (i.e., MY2 and P3), MY2 produces the largest amount of rimed precipitating ice particles, which fall faster than snow (Figures 17c and 17f). The version of P3 used here has one ice category with ice particle riming and deposition affecting the ice density. The P3 fall speed profile therefore resembles the combination of snow above 8-km altitude and partially rimed particles below 8-km altitude (Figures 17b and 17e). Although IWC produced by WSM6 is the smallest, the largest snow mean fall speed and relatively large amount of rimed ice (graupel) lead to an ice particle mass flux comparable to MY2 and P3 right above the melting level. FSBM, which has the smallest ice mass flux among all simulations, produces significant amounts of rimed particles, but they are very small with a mass-weighted mean fall speed of only 0.3–1.3 m/s above 6-km altitude (Figures 17f and S11). The large amount of small hail particles is mainly caused by a very low threshold that was set for liquid particles to form hail through collisions with snow. With this low threshold, snow particles get rimed too quickly before they can grow into relatively large particles, leading to the relatively low number of snow particles as well, particularly for relatively large sizes. In FSBM_NEW, the dominant hydrometeor type is snow with higher mass-weighted mean fall speed compared with FSBM because the snow size distribution is shifted to larger particles (Figure S11). In addition to the higher threshold for liquid-snow collision, less efficient snow breakup also causes greater numbers of large snow particles in FSBM_NEW. As a result, the mean ice particle fall speed in FSBM_NEW is larger than FSBM.

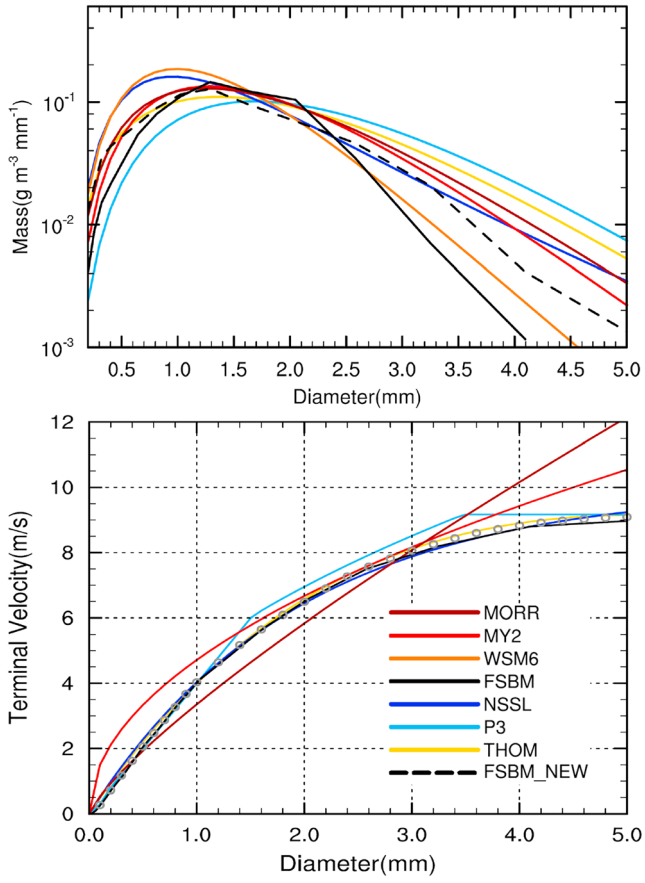

Figure 16. (a) Averaged rain mass size distributions at 2-km altitude and (b) terminal-velocity-size relationship for each scheme. MORR and WSM6 have similar formulations such that their lines are almost overlapped. FSBM and FSBM_NEW have the same values. The gray circle in (b) represents the rain terminal velocity data from Gunn and Kinzer (1949). The data for (a) are processed in the same way as Figure 14.

Stratiform IWC can be produced locally via microphysical processes dominated by deposition (Figure 18a) or advected from the convective region (Figure 18b). Convective condensate detrainment is computed as the total condensate flux across the boundary that approximately separates the convective and stratiform rain rate regions (e.g., the dashed black line in Figure 2) by multiplying total condensate by the horizontal wind

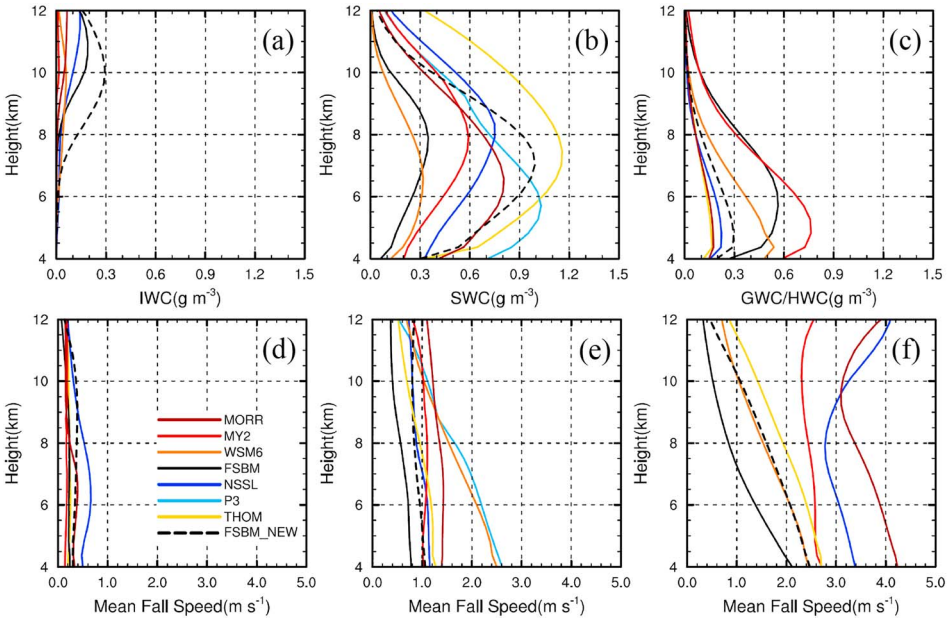

Figure 17. Mean profiles of (a) cloud ice water content (IWC), (b) snow water content (SWC), and (c) graupel/hail water content (GWC/HWC). (d)–(f) show the corresponding mass-weighted mean fall speed for each simulation. The data are processed in the same way as Figure 14. P3 has a single ice category and is plotted in the middle panels.

speed that is perpendicular to the separation line at each grid point for each vertical level. The boundary shown by the dashed black line in Figure 2 approximately represents the convective and stratiform precipitation separation with the surface instantaneous rain rates of 15 mm/hr. To avoid the complexity of finding the exact boundary points, we use this line-shaped boundary for approximation and it should work well for the squall line system. We also keep the boundary constant with height. This assumption should be valid since convection is upright in this squall line case. The total condensate and wind speed are interpolated to the constant height levels with 150-m vertical resolution for this calculation. Note that the total condensate flux does not account for the movement of the squall line. If the movement of squall line is considered, the flux toward the west direction would be even larger, and differences in squall line propagation speed between simulations may further contribute to variability of the condensate fluxes, although this is not analyzed here. However, as shown in Figure 18, the variability of simulated IWC in Figure 14 is very well correlated with the variability of simulated convective condensate detrainment flux (Figure 18b), and the convective condensate detrainment flux variability is primarily determined by total detrained condensate variability since the detrainment wind speed variability is relatively small below 10-km altitude (Figures 18c and 18d). IWC variability is not well correlated with variability in local stratiform IWC net production (Figure 18a), but the IWC magnitude may be modulated by local microphysical processes in some cases. For example, NSSL has relatively weak convective condensate detrainment, but relatively large local ice production rates partly mitigate the weak detrainment (Figure 18a) such that IWC is relatively closer to other simulated IWC values above 7-km altitude in Figure 14d. The magnitude and altitude of the peak detrainment flux do not correlate well with convective updraft strengths presented in Part I. The weak convection group (i.e., NSSL and FSBM) and the strong convection group (i.e., MORR, MY2, and WSM6) analyzed in Part I do not correspond to relatively small and large condensate detrainment fluxes, respectively. It is noted that the much larger ice vertical mass fluxes in FSBM_NEW compared with FSBM are mainly a result of greater convective condensate detrainment fluxes, contributed by greater detrained total condensate.

5.3. Stratiform Precipitation Area

Stratiform precipitation area can also depend on convective condensate detrainment flux, which is largely determined by the detrained total condensate mass from the convective region. Comparing Figure 18b with Figure 4b, a positive correlation between stratiform precipitation area and convective detrainment fluxes is

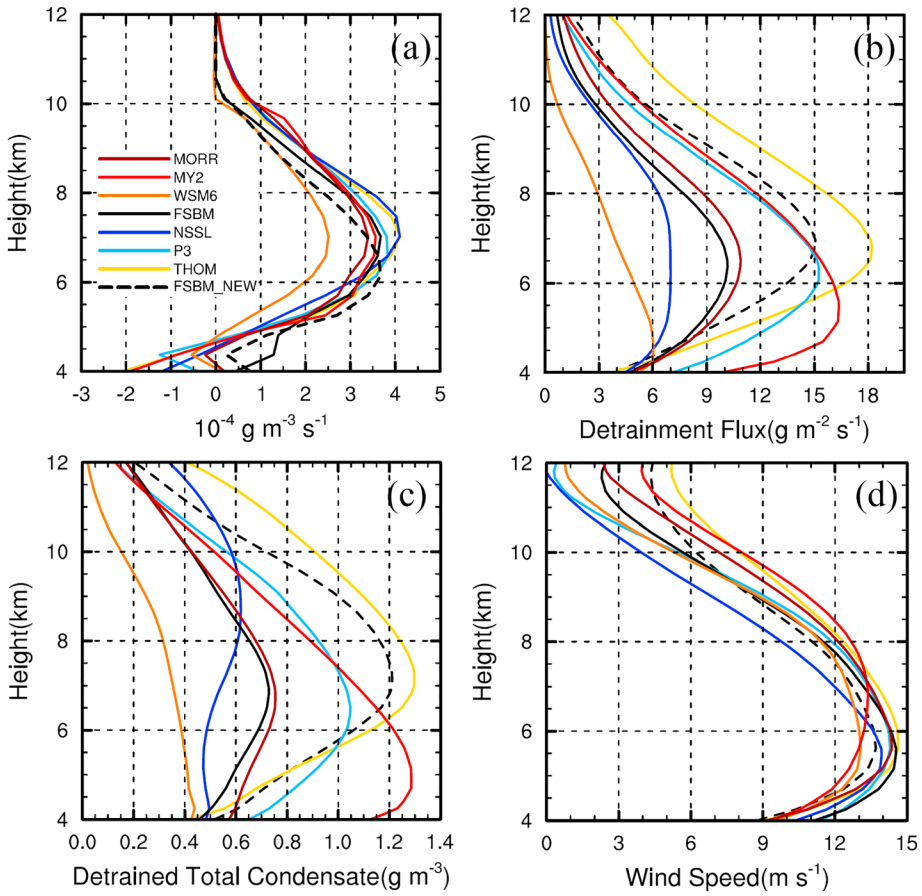

Figure 18. Mean profiles of (a) the sum of all microphysical process rates impacting IWC, (b) the horizontal convective condensate detrainment fluxes, (c) detrained total condensate, and (d) wind speed perpendicular to the separation between the convective and stratiform regions. The convective-stratiform separation is a linear boundary that separates the convective and stratiform rain rate regions, as shown for one time by the dashed black line in Figure 2. This line moves east with the squall line movement to make sure the separation is valid at each 5-min output interval during the analysis time. The data are processed in the same way as Figure 14.

seen. For example, THOM and FSBM_NEW have relatively high values of both quantities, while WSM6 and NSSL are the opposite in both quantities. The correlation coefficient between stratiform precipitation area and the integrated amount of convective condensate detrainment fluxes between 4 and 12 km altitude is 0.78, which is quite high. However, stratiform precipitation area is also found to be modulated by hydrometeor size and fall speed (e.g., Fan et al., 2013; Van Weverberg et al., 2013). For example, MY2 has a relatively large convective condensate detrainment flux, but it produces the largest number of rimed particles with relatively fast fall speeds. Therefore, its stratiform precipitation area is intermediate when compared to other simulations. The relatively large stratiform precipitation areas in THOM, FSBM_NEW, and P3 are also influenced by greater amounts of snow in these schemes compared to other schemes. P3 may simulate both large stratiform precipitation area and rate well because it captures the vertical evolution of hydrometer type well, that is, transitioning from mostly unrimed ice at upper levels to more rimed particles at middle levels right above the melting level.

We find that stratiform precipitation area is also sensitive to the coupling of the simulation with large-scale forcing. As discussed in section 5.1.1, all simulations underestimate stratiform precipitation area. These simulations were carried out using the *nest down* approach with meteorological lateral boundary conditions updated every 3 hr from the outer domain. Based on Figure 4a, three schemes with the median, most, and least underestimation of total stratiform precipitation were chosen to conduct sensitivity tests by changing the lateral boundary condition update frequency from every 3 hr to every 1 hr. These schemes are MORR, NSSL, and P3, and their corresponding sensitivity tests are referred to as MORR_1h, NSSL_1h, and

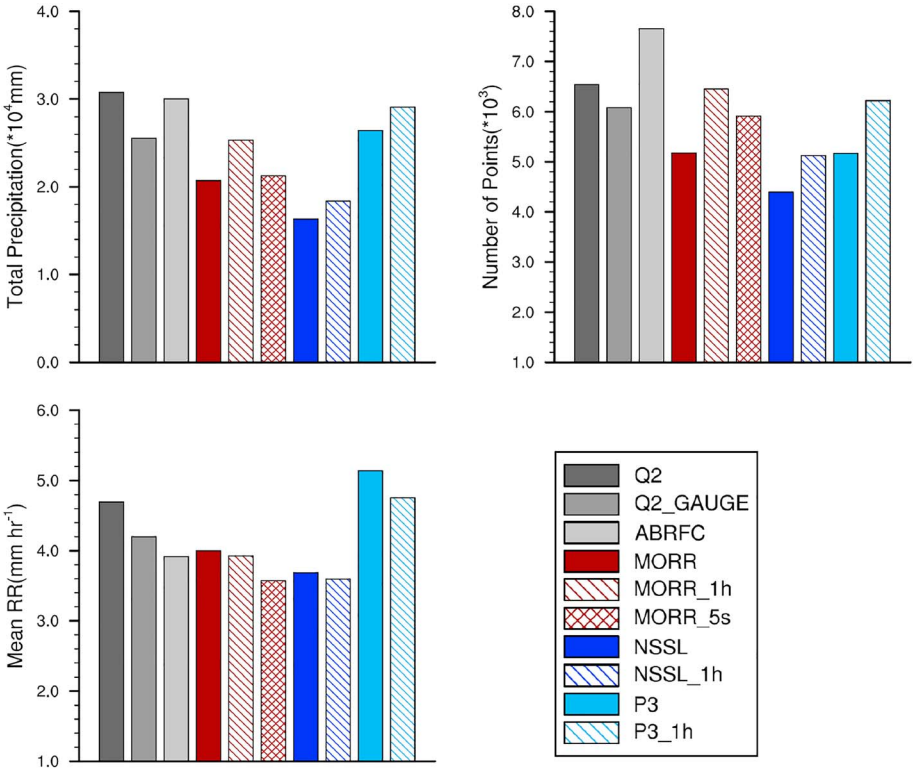

Figure 19. Same as Figure 4, except for the comparisons of MORR, MORR_1h, MORR_5s, NSSL, NSSL_1h, P3, and P3_1h with observations.

P3_1h. Both NSSL (two-moment) and WSM6 (single-moment) have the most underestimation of total stratiform precipitation, and we choose NSSL for the sensitivity test since even climate simulations are already advanced to use two-moment scheme. An additional sensitivity test was conducted with the Morrison scheme using the update frequency of every 5 s (i.e., every model time step), which is referred to as MORR_5s. Figure 19 shows that updating boundary conditions more frequently (meaning a stronger coupling with the large-scale forcing) produces a wider stratiform region as compared with the simulations with boundary conditions updated every 3 hr. An example of such improvement in simulating stratiform region is intuitively shown in spatial distributions of composite radar reflectivity for MORR (Figure S12; similar results with NSSL and P3). Overall, the simulated stratiform precipitation area increases by about 17%–25% and becomes much closer or comparable to observations when increasing the update frequency from every 3 hr to 1 hr (Figure 19). With this increase, we anticipate that the majority of microphysics schemes would not have a significant underestimation of stratiform precipitation area since even for the scheme with the largest underestimation at 3-hr update frequency (i.e., NSSL), with every 1-hr update frequency the underestimation is not much anymore. This suggests that the underestimation of stratiform precipitation area in this study is not only a function of microphysical parameterization and/or convective condensate detrainment flux but also a function of the model domain boundary forcing. Further increasing the boundary condition update frequency to every 5 s does not show noticeable improvement. However, the significant increase of stratiform precipitation area from the 3-hr update frequency to 1-hr update frequency only increases the total stratiform precipitation by about 10%–18%. The mean stratiform rain rate actually slightly decreases (Figure 19c). Therefore, the simulation performances of total stratiform precipitation and mean stratiform rain rate are not necessarily improved significantly. The PDF of stratiform rain rate is not improved much as well (Figure S13). Another reason to use the 3-hr update frequency instead of 1-hr for the study is that more frequent boundary condition update frequency would result in less sensitivity to different microphysical parameterizations.

By examining the meteorological fields at 1000 UTC when the differences in simulated stratiform precipitation area become large, it is shown that the simulations using higher boundary condition update frequency

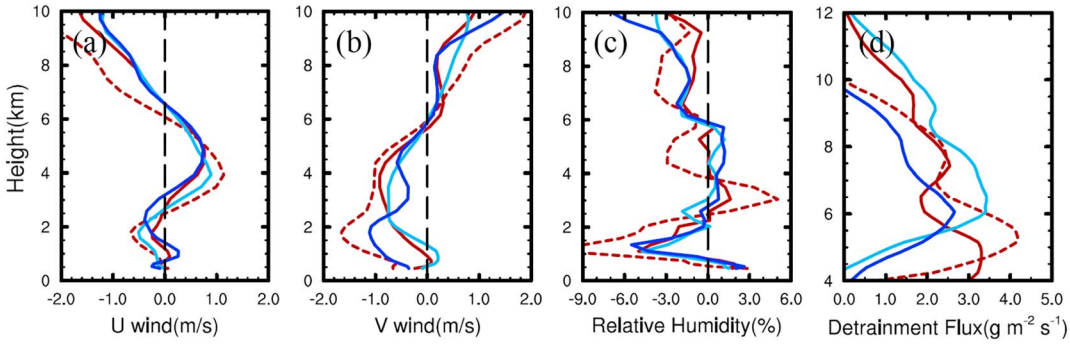

Figure 20. Vertical profiles of differences in (a) *u*-wind, (b) *v*-wind, (c) relative humidity, and (d) convective condensate detrainment flux at 1000 UTC between MORR_1h and MORR (brown solid line), between MORR_5s and MORR (brown dashed line), between NSSL_1h and NSSL (blue line), and between P3_1h and P3 (light blue line). (a) and (b) are averaged over entire domain, whereas (c) is only averaged over the cloud-free points by excluding cloudy grid points (i.e., $Q_{total} < 10^{-6}$ kg/kg). The calculation of convective condensate detrainment flux follows Figure 18b.

produce a stronger easterly wind and stronger southerly wind above 6-km altitude than their 3-hr update frequency counterparts (Figures 20a and 20b). Considering that the simulated squall lines are generally northeast-southwest orientation, this kind of wind field condition is more favorable to the advection of condensate from the convective to the stratiform regions (Figure 20d) and the production of a larger stratiform precipitation area. However, the environmental relative humidity is reduced at most altitudes (Figure 20c), which would increase sublimation and evaporation rates, thus potentially limiting increases in stratiform precipitation. This could partly explain why the simulations with more frequently updated lateral boundary conditions have a relatively limited change in total stratiform precipitation even though they produce significant changes in stratiform precipitation area.

6. Conclusions and Discussion

In this second part of a CRM intercomparison study constrained using the same dynamical model (i.e., WRF-ARW) with eight different cloud microphysics schemes including one-moment bulk, two-moment bulk, and bin parameterizations, the simulated stratiform precipitation properties are compared against observations of a midlatitude squall line event over the U.S. Southern Great Plains on 20 May 2011 during MC3E. The purposes are to examine simulation biases and variability across different microphysics schemes while attempting to understand possible reasons for the biases and variability.

We find that the majority of simulations consistently underestimate total stratiform precipitation primarily due to the underestimation of stratiform precipitation area. All simulations underestimate frequencies of moderate 2–6 mm/hr rain rates, which may result from low-biased ice number and mass concentrations over the 0.2–2-mm diameter range in the stratiform ice region just above the melting level. MY2 and P3 have the largest mean stratiform precipitation rates that exceed those observed, which result from higher than observed frequencies for relatively large rain rates (i.e., 6–10-mm/hr HSRR). WSM6 and FSBM have a low bias in large raindrop concentration at the surface that results from a lack of relatively fast falling large raindrops and too many relatively slow falling small raindrops below 3-km altitude.

The majority of simulations overestimate IWC above 7-km altitude but underestimate IWC right above the melting level, which leads to underestimation of RWC below 3-km altitude because melting is the primary source of stratiform RWC. All simulations fail to simulate the observed increase of IWC as ice approaches the melting level. The overestimation of IWC at upper levels may be related to detrainment that is too high as a result of overestimated convective intensity as shown in Part I, especially since IWC magnitudes correspond well with convective condensate detrainment fluxes. Underestimated IWC just above the melting level could also be related to simulated convective updrafts that are too intense, which detrain condensate and water vapor too high at upper levels increasing the probability that ice particles will excessively sublimate before reaching the melting level. Simulated IWC does, in fact, decrease toward the melting level while observed IWC increases. The evolution of ice number and mass size

distributions between 6.7- and 5.8-km altitudes indicates more efficient ice particle aggregation in observations than simulations, contributing to the disagreement in the shape of simulated and observed ice size distributions. The discrepancy between observed and simulated IWC profiles may be resulted from a combination of deposition that is too weak and sedimentation that is too fast in the simulations, but untangling these two factors requires further information.

We also find that all simulations underestimate descending motion in the stratiform rain region below 3-km altitude, where observed RWC is correlated with descending motion strength. This may be the result of differences in the structure of the rear inflow jet between observations and simulations. The observed jet slowly descends through the observed stratiform region in the form of a mesoscale downdraft, adiabatically warming and drying the air and causing significant rain evaporation. Simulated rear inflow jets remain at relatively lower altitudes such that a robust mesoscale downdraft is not present and evaporation may be limited, as suggested by the less significant decrease in RWC between 3-km altitude and the surface in simulations.

Simulated stratiform precipitation area is positively correlated with convective condensate detrainment flux magnitude. However, the simulated differences in hydrometeor type, size, and fall speed also modulate stratiform precipitation area. Stratiform precipitation area is also sensitive to the coupling of the simulation with large-scale forcing. Simulated stratiform precipitation area using MORR, NSSL, and P3 scheme increases by about 17%–25% and is much closer to observed when the boundary condition update frequency is increased from every 3 to 1 hr. More frequently updated lateral boundary conditions produce more favorable winds aloft for transporting condensate from the convective to the stratiform regions, thus producing a larger stratiform area, but the underprediction of mean stratiform precipitation rate is not improved.

The spread in stratiform precipitation properties (i.e., area, rate, and total precipitation) across the schemes is about a factor of 1.5, generally similar to that of convective intensity and precipitation in Part I. The simulated rain rate variability is determined by the variability of both the rain mass-weighted mean fall speed and RWC. The spread of rain mass-weighted mean fall speed is primarily a function of differences in simulated raindrop size distributions. RWC variability is impacted by differences in melting and rain evaporation rates, with the melting rate variations strongly affected by differences in downward ice mass fluxes directly above the melting level. Ice particle mass fluxes vary by up to a factor of 2. For most schemes, this significant variability is caused by differences in both IWC related to convective condensate detrainment flux variability and differences in ice mass-weighted mean fall speeds related to different proportions of ice types and their assumed properties.

Overall, these results indicate that the magnitude and variability of stratiform precipitation among schemes are ultimately related to the magnitude and variability of ice particle mass fluxes above the melting level. These fluxes are significantly impacted by the kinematic and microphysical properties of convective regions, which are the primary source for ice in the stratiform region, while local ice growth processes in the stratiform region play a secondary role in model spread. These results suggest that accurate simulation of convective regions is critical to better simulating stratiform precipitation, and therefore, future observations should target convective dynamics and microphysics such that models can be more extensively evaluated and improved. This point is also highlighted by Varble et al. (2014a, 2014b) for a tropical MCS event; however, further cases should be analyzed in the future to determine the generality.

Based on our intercomparison study in both convective and stratiform regions (Part I in Fan et al., 2017 and Part II here), the single-moment scheme WSM6 has the largest overestimation of convective intensity and the largest underestimation of stratiform precipitation area and total stratiform precipitation among all the schemes. Therefore, increasing the complexity from single-moment to double-moment parameterization clearly helps improve model performance, which was shown from previous studies as well (e.g., Morrison et al., 2009). As for further increasing the complexity from two-moment to bin scheme, the advantage in performance is not that clear in this case. This is not surprising because (1) the study case is ice microphysics dominated, while our understanding about many ice microphysical processes is very limited. As revealed in Part I, ice microphysics is responsible for the large model spread in convective intensity across the schemes; and (2) it is not a case occurring in a very polluted environment or significantly influenced by aerosol plumes during the convective development. The amount of cloud condensation nuclei (CCN) and ice

nucleating particles (INP) can be significant factors impacting cloud and precipitation properties under polluted conditions. The current two-moment bulk schemes are not designed well to handle the response of microphysical processes to CCN and INP (see details in Fan et al., 2016). Therefore, with the current understanding, using more detailed parameterization of microphysics can help only when there are sufficient observations to constrain parameters such as those associated with collision/breakup processes and CCN/INP properties.

Acknowledgments
This study was supported by the U.S. Department of Energy (DOE) Atmospheric System Research (ASR) Program and the Climate Model Development and Validation (CMDV) program. The Pacific Northwest National Laboratory (PNNL) is operated for the DOE by Battelle Memorial Institute under contract DE-AC06-76RLO1830. This research used PNNL Institutional Computing resources and also resources at the National Energy Research Scientific Computing Center, which is supported by the Office of Science of the U.S. DOE under contract DE-AC02-05CH1123. Bin Han and Dr. Chen were supported by the National Basic Research Program of China (2013CB430105) and the National Natural Science Foundation of China (41575130 and 41775132). Dr. Varble was supported by U.S. DOE ASR grant DE-SC0008678. Dr. Morrison was supported by U.S. DOE ASR grant DE-SC0008648. Drs. Morrison and Varble were also supported by U.S. DOE ASR grant DE-SC0016476. Dr. Dong was supported by DOE CMDV project at University of Arizona with award number DE-SC0017015. Dr. Giangrande is an employee of Brookhaven Science Associates, LLC, under contract DE-AC02-98CH10886 with the U.S. DOE. Prof. Alexander Khain and Jacob Shpund are supported by grant DE-SC008811 and the Israel Science Foundation grant 2027/17.The National Center for Atmospheric Research is sponsored by the U.S. National Science Foundation. The simulation data are available at http://portal.nersc.gov/project/m2689/evaluation/. We also acknowledge the Atmospheric Radiation Measurement (ARM) Climate Research Facility, a user facility of the U.S. DOE, as well as the MC3E team for the field data. DOE ARM data sets used in this study can be obtained from the ARM Archive at http://www.arm.gov and ARM External Data Center at https://www.arm.gov/xdc/.

References

Bernardet, L. R., Grasso, L. D., Nachamkin, J. E., Finley, C. A., & Cotton, W. R. (2000). Simulating convective events using a high-resolution mesoscale model. *Journal of Geophysical Research*, *105*(D11), 14,963–14,982. https://doi.org/10.1029/2000JD900100

Biggerstaff, M. I., & Houze, R. A. Jr. (1991). Kinematic and precipitation structure of the 10–11 June 1985 squall line. *Monthly Weather Review*, *119*(12), 3034–3065. https://doi.org/10.1175/1520-0493(1991)119<3034:KAPSOT>2.0.CO;2

Blossey, P. N., Bretherton, C. S., Cetrone, J., & Kharoutdinov, M. (2007). Cloud-resolving model simulations of KWAJEX: Model sensitivities and comparisons with satellite radar observations. *Journal of the Atmospheric Sciences*, *64*(5), 1488–1508. https://doi.org/10.1175/JAS3982.1

Braun, S. A., & Houze, R. A. Jr. (1994). The transition zone and secondary maximum of radar reflectivity behind a midlatitude squall line: Results retrieved from Doppler radar data. *Journal of the Atmospheric Sciences*, *51*(19), 2733–2755. https://doi.org/10.1175/1520-0469(1994)051<2733:TTZASM>2.0.CO;2

Brown, B. R., Bell, M. M., & Thompson, G. (2017). Improvements to the snow melting process in a partially double moment microphysics parameterization. *Journal of Advances in Modeling Earth Systems*, *9*, 1150–1166. https://doi.org/10.1002/2016MS000892

Bryan, G. H., & Morrison, H. (2012). Sensitivity of a simulated squall line to horizontal resolution and parameterization of microphysics. *Monthly Weather Review*, *140*(1), 202–225. https://doi.org/10.1175/MWR-D-11-00046.1

Churchill, D. D., & Houze, R. A. Jr. (1984). Development and structure of winter monsoon cloud clusters on 10 December 1978. *Journal of the Atmospheric Sciences*, *41*(6), 933–960. https://doi.org/10.1175/1520-0469(1984)041<0933:DASOWM>2.0.CO;2

Fan, J., Han, B., Varble, A., Morrison, H., North, K., Kollias, P., Chen, B., et al. (2017). Cloud-resolving model intercomparison of an MC3E squall line case: Part I—Convective updrafts. *Journal of Geophysical Research: Atmospheres*, *122*, 9351–9378. https://doi.org/10.1002/2017JD026622

Fan, J., Leung, L. R., Rosenfeld, D., Chen, Q., Li, Z., Zhang, J., & Yan, H. (2013). Microphysical effects determine macrophysical response for aerosol impact on deep convective clouds. *Proceedings of the National Academy of Sciences of the United States of America*, *110*(48), E4581–E4590. https://doi.org/10.1073/pnas.1316830110

Fan, J., Liu, Y.-C., Xu, K.-M., North, K., Collis, S., Dong, X., et al. (2015). Improving representation of convective transport for scale-aware parameterization: 1. Convection and cloud properties simulated with spectral bin and bulk microphysics. *Journal of Geophysical Research: Atmospheres*, *120*, 3485–3509. https://doi.org/10.1002/2014JD022142

Fan, J., Rosenfeld, D., Ding, Y., Leung, L. R., & Li, Z. (2012). Potential aerosol indirect effects on atmospheric circulation and radiative forcing through deep convection. *Geophysical Research Letters*, *39*, L09806. https://doi.org/10.1029/2012GL051851

Fan, J., Wang, Y., Rosenfeld, D., & Liu, X. (2016). Review of aerosol–cloud interactions: Mechanisms, significance, and challenges. *Journal of the Atmospheric Sciences*, *73*(11), 4221–4252. https://doi.org/10.1175/JAS-D-16-0037.1

Ferrier, B. S., Simpson, J., & Tao, W.-K. (1996). Factors responsible for different precipitation efficiencies between midlatitude and tropical squall simulations. *Monthly Weather Review*, *124*(10), 2100–2125. https://doi.org/10.1175/1520-0493(1996)124<2100:FRFPEI>2.0.CO;2

Fovell, R. G., & Ogura, Y. (1988). Numerical simulation of a midlatitude squall line in two dimensions. *Journal of the Atmospheric Sciences*, *45*(24), 3846–3879. https://doi.org/10.1175/1520-0469(1988)045<3846:NSOAMS>2.0.CO;2

Franklin, C. N., Protat, A., Leroy, D., & Fontaine, E. (2016). Controls on phase composition and ice water content in a convection-permitting model simulation of a tropical mesoscale convective system. *Atmospheric Chemistry and Physics*, *16*(14), 8767–8789. https://doi.org/10.5194/acp-16-8767-2016

Fridlind, A. M., Li, X., Wu, D., van Lier-Walqui, M., Ackerman, A. S., Tao, W. K., et al. (2017). Derivation of aerosol profiles for MC3E convection studies and use in simulations of the 20 May squall line case. *Atmospheric Chemistry and Physics*, *17*(9), 5947–5972. https://doi.org/10.5194/acp-17-5947-2017

Giangrande, S. E., Collis, S., Straka, J., Protat, A., Williams, C., & Krueger, S. (2013). A summary of convective-core vertical velocity properties using ARM UHF wind profilers in Oklahoma. *Journal of Applied Meteorology and Climatology*, *52*(10), 2278–2295. https://doi.org/10.1175/JAMC-D-12-0185.1

Giangrande, S. E., Collis, S., Theisen, A. K., & Tokay, A. (2014). Precipitation estimation from the ARM distributed radar network during theMC3E campaign. *Journal of Applied Meteorology and Climatology*, *53*(9), 2130–2147. https://doi.org/10.1175/JAMC-D-13-0321.1

Giangrande, S. E., & Ryzhkov, A. V. (2008). Estimation of rainfall based on the results of polarimetric echo classification. *Journal of Applied Meteorology and Climatology*, *47*(9), 2445–2462. https://doi.org/10.1175/2008JAMC1753.1

Giangrande, S. E., Toto, T., Bansemer, A., Kumjian, M. R., Mishra, S., & Ryzhkov, A. V. (2016). Insights into riming and aggregation processes as revealed by aircraft, radar, and disdrometer observations for a27 April 2011 widespread precipitation event. *Journal of Geophysical Research: Atmospheres*, *121*, 5846–5863. https://doi.org/10.1002/2015JD024537

Gourley, J. J., Giangrande, S. E., Hong, Y., Flaming, Z., Schuur, T., & Vrugt, J. A. (2010). Impacts of polarimetric radar observations on hydrologic simulation. *Journal of Hydrometeorology*, *11*(3), 781–796. https://doi.org/10.1175/2010JHM1218.1

Gunn, R., & Kinzer, G. D. (1949). The terminal velocity of fall for water drops in stagnant air. *Journal of Meteorology*, *6*(4), 243–248. https://doi.org/10.1175/1520-0469(1949)006<0243:TTVOFF>2.0.CO;2

Hong, S.-Y., & Lim, J.-O. J. (2006). The WRF single-moment 6-class microphysics scheme (WSM6). *Journal of the Korean Meteorological Society*, *42*, 129–151.

Houze, R. A. Jr. (1977). Structure and dynamics of a tropical squall-line system. *Monthly Weather Review*, *105*(12), 1540–1567. https://doi.org/10.1175/1520-0493(1977)105<1540:SADOAT>2.0.CO;2

Houze, R. A. Jr. (2004). Mesoscale convective systems. *Reviews of Geophysics*, *42*, RG4003. https://doi.org/10.1029/2004RG000150

Jensen, M., Petersen, W. A., Bansemer, A., Bharadwaj, N., Carey, L. D., Cecil, D. J., et al. (2016). The Midlatitude Continental Convective Clouds Experiment (MC3E). *Bulletin of the American Meteorological Society*, *97*(9), 1667–1686. https://doi.org/10.1175/BAMS-D-14-00228.1

Khain, A. P. (2009). Notes on state-of-art investigations of aerosol effects on precipitation: A critical review. *Environmental Research Letters*, *4*(1), 015004. https://doi.org/10.1088/1748-9326/4/1/015004

Khain, A. P., Beheng, K. D., Heymsfield, A., Korolev, A., Krichak, S. O., Levin, Z., et al. (2015). Representation of microphysical processes in cloud-resolving models: Spectral (bin) microphysics versus bulk parameterization. *Reviews of Geophysics*, *53*, 247–322. https://doi.org/10.1002/2014RG000468

Korolev, A., Strapp, J. W., Isaac, G. A., & Emery, E. (2013). Improved airborne hot-wire measurements of ice water content in clouds. *Journal of Atmospheric and Oceanic Technology*, *30*(9), 2121–2131. https://doi.org/10.1175/JTECH-D-13-00007.1

Korolev, A. V., Strapp, J. W., & Isaac, G. A. (1998). Evaluation of the accuracy of PMS optical array probes. *Journal of Atmospheric and Oceanic Technology*, *15*(3), 708–720. https://doi.org/10.1175/1520-0426(1998)015<0708:EOTAOP>2.0.CO;2

Kumjian, M. R., Mishra, S., Giangrande, S. E., Toto, T., Ryzhkov, A. V., & Bansemer, A. (2016). Polarimetric radar and aircraft observations of saggy bright bands during MC3E. *Journal of Geophysical Research: Atmospheres*, *121*, 3584–3607. https://doi.org/10.1002/2015JD024446

Lang, S., Tao, W.-K., Simpson, J., Cifelli, R., Rutledge, S., Olson, W., & Halverson, J. (2007). Improving simulations of convective systems from TRMM LBA: Easterly and westerly regimes. *Journal of the Atmospheric Sciences*, *64*(4), 1141–1164. https://doi.org/10.1175/JAS3879.1

Lang, S., Tao, W.-K., Simpson, J., & Ferrier, B. (2003). Modeling of convective-stratiform precipitation processes: Sensitivity to partitioning methods. *Journal of Applied Meteorology*, *42*(4), 505–527. https://doi.org/10.1175/1520-0450(2003)042<0505:MOCSPP>2.0.CO;2

Li, X., Tao, W.-K., Khain, A. P., Simpson, J., & Johnson, D. E. (2009). Sensitivity of a cloud-resolving model to bulk and explicit bin microphysical schemes. Part I: Validation with a PRE-STORM case. *Journal of the Atmospheric Sciences*, *66*(1), 3–21. https://doi.org/10.1175/2008JAS2646.1

Li, Y., Zipser, E. J., Krueger, S. K., & Zulauf, M. A. (2008). Cloud-resolving modeling of deep convection during KWAJEX. Part I: Comparison to TRMM satellite and ground-based observations. *Monthly Weather Review*, *136*(7), 2699–2712. https://doi.org/10.1175/2007MWR2258.1

Liu, C., & Zipser, E. J. (2013). Why does radar reflectivity tend to increase downward toward the ocean surface, but decrease downward toward the land surface? *Journal of Geophysical Research: Atmospheres*, *118*, 135–148. https://doi.org/10.1029/2012JD018134

Luo, Y., Wang, Y., Wang, H., Zheng, Y., & Morrison, H. (2010). Modeling convective-stratiform precipitation processes on a Mei-Yu front with the Weather Research and Forecasting model: Comparison with observations and sensitivity to cloud microphysics parameterizations. *Journal of Geophysical Research*, *115*, D18117. https://doi.org/10.1029/2010JD013873

Mansell, E. R., Ziegler, C. L., & Bruning, E. C. (2010). Simulated electrification of a small thunderstorm with two-moment bulk microphysics. *Journal of the Atmospheric Sciences*, *67*(1), 171–194. https://doi.org/10.1175/2009JAS2965.1

Marinescu, P. J., van den Heever, S. C., Saleeby, S. M., & Kreidenweis, S. M. (2016). The microphysical contributions to and evolution of latent heating profiles in two MC3E MCSs. *Journal of Geophysical Research: Atmospheres*, *121*, 7913–7935. https://doi.org/10.1002/2016JD024762

Mather, J. H., & Voyles, J. W. (2013). The ARM climate research facility: A review of structure and capabilities. *Bulletin of the American Meteorological Society*, *94*(3), 377–392. https://doi.org/10.1175/BAMS-D-11-00218.1

McCumber, M., Tao, W.-K., Simpson, J., Penc, R., & Soong, S.-T. (1991). Comparison of ice-phase microphysical parameterization schemes using numerical simulations of tropical convection. *Journal of Applied Meteorology*, *30*(7), 985–1004. https://doi.org/10.1175/1520-0450-30.7.985

Milbrandt, J. A., Glazer, A., & Jacob, D. (2012). Predicting the snow-to-liquid ratio of surface precipitation using a bulk microphysics scheme. *Monthly Weather Review*, *140*(8), 2461–2476. https://doi.org/10.1175/MWR-D-11-00286.1

Milbrandt, J. A., & McTaggart-Cowan, R. (2010). Sedimentation-induced errors in bulk microphysics schemes. *Journal of the Atmospheric Sciences*, *67*(12), 3931–3948. https://doi.org/10.1175/2010JAS3541.1

Milbrandt, J. A., & Yau, M. K. (2005a). A multimoment bulk microphysics parameterization. Part I: Analysis of the role of the spectral shape parameter. *Journal of the Atmospheric Sciences*, *62*(9), 3051–3064. https://doi.org/10.1175/JAS3534.1

Milbrandt, J. A., & Yau, M. K. (2005b). A multimoment bulk microphysics parameterization. Part II: A proposed three-moment closure and scheme description. *Journal of the Atmospheric Sciences*, *62*(9), 3065–3081. https://doi.org/10.1175/JAS3535.1

Morrison, H., Curry, J. A., & Khvorostyanov, V. I. (2005). A new double-moment microphysics parameterization for application in cloud and climate models. Part I: Description. *Journal of the Atmospheric Sciences*, *62*(6), 1665–1677. https://doi.org/10.1175/JAS3446.1

Morrison, H., & Milbrandt, J. A. (2015). Parameterization of cloud microphysics based on the prediction of bulk ice particle properties. Part I: Scheme description and idealized tests. *Journal of the Atmospheric Sciences*, *72*(1), 287–311. https://doi.org/10.1175/JAS-D-14-0065.1

Morrison, H., Milbrandt, J. A., Bryan, G. H., Ikeda, K., Tessendorf, S. A., & Thompson, G. (2015). Parameterization of cloud microphysics based on the prediction of bulk ice particle properties. Part II: Case study comparisons with observations and other schemes. *Journal of the Atmospheric Sciences*, *72*(1), 312–339. https://doi.org/10.1175/JAS-D-14-0066.1

Morrison, H., Thompson, G., & Tatarskii, V. (2009). Impact of cloud microphysics on the development of trailing stratiform precipitation in a simulated squall line: Comparison of one- and two-moment schemes. *Monthly Weather Review*, *137*(3), 991–1007. https://doi.org/10.1175/2008MWR2556.1

Newsom, R. K., Turner, D. D., & Goldsmith, J. E. M. (2013). Long-term evaluation of temperature profiles measured by an operational Raman lidar. *Journal of Atmospheric and Oceanic Technology*, *30*(8), 1616–1634. https://doi.org/10.1175/JTECH-D-12-00138.1

North, K. W., Oue, M., Kollias, P., Giangrande, S. E., Collis, S., & Potvin, C. K. (2017). Vertical air motion retrievals in deep convective clouds using the ARM scanning radar network in Oklahoma during MC3E. *Atmospheric Measurement Techniques*, *10*, 2785–2806. https://doi.org/10.5194/amt-10-2785-2017

Parker, M. D., & Johnson, R. H. (2000). Organizational modes of midlatitude mesoscale convective systems. *Monthly Weather Review*, *128*(10), 3413–3436. https://doi.org/10.1175/1520-0493(2001)129<3413:OMOMMC>2.0.CO;2

Rutledge, S. A., & Houze, R. A. (1987). A diagnostic modelling study of the trailing stratiform region of a midlatitude squall line. *Journal of the Atmospheric Sciences*, *44*(18), 2640–2656. https://doi.org/10.1175/1520-0469(1987)044,2640:ADMSOT.2.0.CO;2

Ryzhkov, A. V., Giangrande, S. E., & Schuur, T. J. (2005). Rainfall estimation with a polarimetric prototype of WSR-88D. *Journal of Applied Meteorology*, *44*(4), 502–515. https://doi.org/10.1175/JAM2213.1

Schönhuber, M., Lammer, G., & Randeu, W. L. (2008). The 2D video distrometer. In S. Michaelides (Ed.), *Precipitation: Advances in measurement, estimation and prediction* (pp. 3–31). Berlin, Heidelberg: Springer.

Skamarock,W. C., Klemp, J. B., Dudhia, J., Gill, D. O., Barker, D. M., Duda, M. G., et al. (2008). A description of the Advanced Research WRF version 3, Tech. Note NCAR/TN-475+STR.

Smith, A. M., McFarquhar, G. M., Rauber, R. M., Grim, J. A., Timlin, M. S., & Jewett, B. F. (2009). Microphysical and thermodynamic structure and evolution of the trailing stratiform regions of mesoscale convective systems during BAMEX. Part I: Observations. *Monthly Weather Review*, *137*(4), 1165–1185. https://doi.org/10.1175/2008MWR2504.1

Smull, B. F., & Houze, R. A. (1987). Dual-Doppler radar analysis of a midlatitude squall line with a trailing region of stratiform rain. *Journal of the Atmospheric Sciences*, *44*(15), 2128–2149. https://doi.org/10.1175/1520-0469(1987)044<2128:DDRAOA>2.0.CO;2

Stanford, M. W., Varble, A., Zipser, E., Strapp, J. W., Leroy, D., Schwarzenboeck, A., et al. (2017). A ubiquitous ice size bias in simulations of tropical deep convection. *Atmospheric Chemistry and Physics*, *17*(15), 9599–9621. https://doi.org/10.5194/acp-17-9599-2017

Steiner, M., Houze, R., & Yuter, S. E. (1995). Climatological characterization of three-dimensional storm structure from operational radar and rain gauge data. *Journal of Applied Meteorology*, *34*(9), 1978–2007. https://doi.org/10.1175/1520-0450(1995)034<1978:CCOTDS>2.0.CO;2

Stenz, R., Dong, X., Xi, B., & Kuligowski, B. (2014). Assessment of SCaMPR and NEXRAD Q2 precipitation estimates using Oklahoma Mesonet observations. *Journal of Hydrometeorology*, *15*(6), 2484–2500. https://doi.org/10.1175/JHM-D-13-0199.1

Tao, W.-K., Sui, C.-H., Ferrier, B., Lang, S., Scala, J., Chou, M.-D., & Pickering, K. (1993). Heating, moisture and water budgets of tropical and midlatitude squall lines. Comparisons and sensitivity to longwave radiation. *Journal of the Atmospheric Sciences*, *50*(5), 673–690. https://doi.org/10.1175/1520-0469(1993)050<0673:HMAWBO>2.0.CO;2

Tao, W.-K., Wu, D., Lang, S., Chern, J.-D., Peters-Lidard, C., Fridlind, A., & Matsui, T. (2016). High-resolution NU-WRF simulations of a deep convective-precipitation system during MC3E: Further improvements and comparisons between Goddard microphysics schemes and observations. *Journal of Geophysical Research: Atmospheres*, *121*, 1278–1305. https://doi.org/10.1002/2015JD023986

Thompson, G., Field, P. R., Rasmussen, R. M., & Hall, W. D. (2008). Explicit forecasts of winter precipitation using an improved bulk microphysics scheme. Part II: Implementation of a new snow parameterization. *Monthly Weather Review*, *136*(12), 5095–5115. https://doi.org/10.1175/2008MWR2387.1

Thompson, G., Rasmussen, R. M., & Manning, K. (2004). Explicit forecasts of winter precipitation using an improved bulk microphysics scheme. Part I: Description and sensitivity analysis. *Monthly Weather Review*, *132*(2), 519–542. https://doi.org/10.1175/1520-0493(2004)132<0519:EFOWPU>2.0.CO;2

Thurai, M., Petersen, W. A., Tokay, A., Schultz, C., & Gatlin, P. (2011). Drop size distribution comparisons between Parsivel and 2D video disdrometers. *Advances in Geosciences*, *30*, 3–9. https://doi.org/10.5194/adgeo-30-3-2011

Tian, J., Dong, X., Xi, B., Wang, J., Homeyer, C. R., McFarquhar, G. M., & Fan, J. (2016). Retrievals of ice cloud microphysical properties of deep convective systems using radar measurements. *Journal of Geophysical Research: Atmospheres*, *121*, 10,820–10,839. https://doi.org/10.1002/2015JD024686

Tokay, A., D'Adderio, L. P., Porcù, F., Wolff, D. B., & Petersen, W. A. (2017). A field study of footprint-scale variability of raindrop size distribution. *Journal of Hydrometeorology*, *18*(12), 3165–3179. https://doi.org/10.1175/JHM-D-17-0003.1

Tokay, A., Petersen, W. A., Gatlin, P., & Wingo, M. (2013). Comparison of raindrop size distribution measurements by collocated disdrometers. *Journal of Atmospheric and Oceanic Technology*, *30*(8), 1672–1690. https://doi.org/10.1175/JTECH-D-12-00163.1

Van Weverberg, K., Vogelmann, A. M., Lin, W., Luke, E. P., Cialella, A., Minnis, P., et al. (2013). The role of cloud microphysics parameterization in the simulation of mesoscale convective system clouds and precipitation in the tropical western Pacific. *Journal of the Atmospheric Sciences*, *70*(4), 1104–1128. https://doi.org/10.1175/JAS-D-12-0104.1

Varble, A., Fridlind, A. M., Zipser, E. J., Ackerman, A. S., Chaboureau, J.-P., Fan, J., et al. (2011). Evaluation of cloud-resolving model intercomparison simulations using TWP-ICE observations: Precipitation and cloud structure. *Journal of Geophysical Research*, *116*, D12206. https://doi.org/10.1029/2010JD015180

Varble, A., Zipser, E. J., Fridlind, A. M., Zhu, P., Ackerman, A. S., Chaboureau, J.-P., et al. (2014a). Evaluation of cloud-resolving and limited area model intercomparison simulations using TWP-ICE observations: 1. Deep convective updraft properties. *Journal of Geophysical Research: Atmospheres*, *119*, 13,891–13,918. https://doi.org/10.1002/2013JD021371

Varble, A., Zipser, E. J., Fridlind, A. M., Zhu, P., Ackerman, A. S., Chaboureau, J.-P., et al. (2014b). Evaluation of cloud-resolving and limited area model intercomparison simulations using TWP-ICE observations: 2. Precipitation microphysics. *Journal of Geophysical Research: Atmospheres*, *119*, 13,919–13,945. https://doi.org/10.1002/2013JD021372

Wang, J., Dong, X., & Xi, B. (2015). Investigation of ice cloud microphysical properties of DCSs using aircraft in situ measurements during MC3E over the ARM SGP site. *Journal of Geophysical Research: Atmospheres*, *120*, 3533–3552. https://doi.org/10.1002/2014JD022795

Wang, J., Dong, X., & Xi, B. (2018). Investigation of liquid cloud microphysical properties of deep convective systems: 2. Parameterization of raindrop size distribution and its application for convective rain estimation. *Journal of Geophysical Research: Atmospheres*, *123*, 11,637–11,651. https://doi.org/10.1029/2018JD028727

Wang, J., Dong, X., Xi, B., & Heymsfield, A. J. (2016). Investigation of liquid cloud microphysical properties of deep convective systems: 1. Parameterization of raindrop size distribution and its application for stratiform rain estimation. *Journal of Geophysical Research: Atmospheres*, *121*, 10,739–10,760. https://doi.org/10.1002/2016JD024941

Weisman, M. L., Davis, C., Wang, W., Manning, K. W., & Klemp, J. B. (2008). Experiences with 0–36 h explicit convective forecasts with the WRF-ARW model. *Weather Forecasting*, *23*(3), 407–437. https://doi.org/10.1175/2007WAF2007005.1

Whiton, R. C., Smith, P. L., Bigler, S. G., Wilk, K. E., & Harbuck, A. C. (1998). History of operational use of weather radar by U.S. weather services. Part II: Development of operational Doppler weather radars. *Weather Forecasting*, *13*(2), 244–252. https://doi.org/10.1175/1520-0434(1998)013<0244:HOOUOW>2.0.CO;2

Williams, C. R. (2012). Vertical air motion retrieved from dual-frequency profiler observations. *Journal of Atmospheric and Oceanic Technology*, *29*(10), 1471–1480. https://doi.org/10.1175/JTECH-D-11-00176.1

Williams, C. R. (2016). Reflectivity and liquid water content vertical decomposition diagrams to diagnose vertical evolution of raindrop size distributions. *Journal of Atmospheric and Oceanic Technology*, *33*(3), 579–595. https://doi.org/10.1175/JTECH-D-15-0208.1

Williams, C. R., & Gage, K. S. (2009). Raindrop size distribution variability estimated using ensemble statistics. *Annales de Geophysique*, *27*(2), 555–567. https://doi.org/10.5194/angeo-27-555-2009

Wu, D., Dong, X., Xi, B., Feng, Z., Kennedy, A., Mullendore, G., et al. (2013). Impacts of microphysical scheme on convective and stratiform characteristics in two high precipitation squall line events. *Journal of Geophysical Research: Atmospheres*, *118*, 11,119–11,135. https://doi.org/10.1002/jgrd.50798

Xu, K. M., Cederwall, R. T., Donner, L. J., Grabowski, W. W., Guichard, F., Johnson, D. E., et al. (2002). An intercomparison of cloud-resolving models with the atmospheric radiation measurement summer 1997 intensive observation period data. *Quarterly Journal of the Royal Meteorological Society*, *128*(580), 593–624. https://doi.org/10.1256/003590002321042117

Young, C. B., Bradley, A. A., Krajewski, W. F., Kruger, A., & Morrissey, M. L. (2000). Evaluating NEXRAD multisensor precipitation estimates for operational hydrologic forecasting. *Journal of Hydrometeorology*, *1*(3), 241–254. https://doi.org/10.1175/1525-7541(2000)001<0241:ENMPEF>2.0.CO;2

Zhang, J., Howard, K., Langston, C., Vasiloff, S., Kaney, B., Arthur, A., et al. (2011). National mosaic and multi-sensor QPE (NMQ) system: Description, results, and future plans. *Bulletin of the American Meteorological Society*, *92*(10), 1321–1338. https://doi.org/10.1175/2011BAMS-D-11-00047.1